Macromolecules

Subscriber access provided by MIT

Article

End-Monomer Dynamics in Semiflexible Polymers

Michael Hinczewski, Xaver Schlagberger, Michael Rubinstein, Oleg Krichevsky, and Roland R. Netz

Macromolecules, **2009**, 42 (3), 860-875• DOI: 10.1021/ma802017g • Publication Date (Web): 15 January 2009

Downloaded from http://pubs.acs.org on March 28, 2009

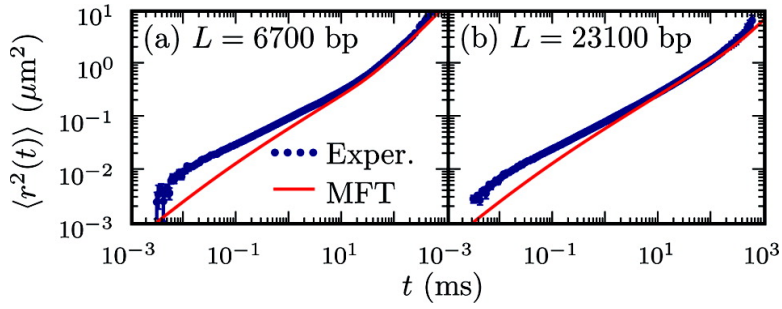

More About This Article

Additional resources and features associated with this article are available within the HTML version:

- Supporting Information
- Access to high resolution figures
- Links to articles and content related to this article
- Copyright permission to reproduce figures and/or text from this article

View the Full Text HTML

ACS Publications
High quality. High impact.

Macromolecules is published by the American Chemical Society. 1155 Sixteenth Street N.W., Washington, DC 20036

End-Monomer Dynamics in Semiflexible Polymers

Michael Hinczewski,*,† Xaver Schlagberger,‡ Michael Rubinstein,§ Oleg Krichevsky,⊥ and Roland R. Netz‡

Feza Gürsey Research Institute, TÜBITAK - Bosphorus University, Çengelköy 34684, Istanbul, Turkey; Physics Department, Technical University of Munich, 85748 Garching, Germany; Department of Chemistry, University of North Carolina, Chapel Hill, North Carolina 27599-3290; and Physics Department, Ben-Gurion University, Beer-Sheva 84105, Israel

Received September 3, 2008; Revised Manuscript Received October 29, 2008

ABSTRACT: Spurred by an experimental controversy in the literature, we investigate the end-monomer dynamics of semiflexible polymers through Brownian hydrodynamic simulations and dynamic mean-field theory. Precise experimental observations over the past few years of end-monomer dynamics in the diffusion of double-stranded DNA have given conflicting results: one study indicated an unexpected Rouse-like scaling of the mean-squared displacement (MSD) $\langle r^2(t)\rangle \sim t^{1/2}$ at intermediate times, corresponding to fluctuations at length scales larger than the persistence length but smaller than the coil size; another study claimed the more conventional Zimm scaling $\langle r^2(t)\rangle \sim t^{2/3}$ in the same time range. Using hydrodynamic simulations as well as analytical and scaling theories, we find a novel intermediate dynamical regime where the effective local exponent of the end-monomer MSD, $\alpha(t) = \mathrm{d}(\log\langle r^2(t)\rangle)/\mathrm{d}(\log t)$ drops below the Zimm value of 2/3 for sufficiently long chains. The deviation from the Zimm prediction increases with chain length, though it does not reach the Rouse limit of 1/2. The qualitative features of this intermediate regime, found in simulations and in an improved mean-field theory for semiflexible polymers, in particular the variation of $\alpha(t)$ with chain and persistence lengths, can be reproduced through a heuristic scaling argument. Anomalously low values of the effective exponent α are explained by hydrodynamic effects related to the slow crossover from dynamics on length scales smaller than the persistence length to dynamics on larger length scales.

1. Introduction

Recent experimental advances using fluorescence correlation spectroscopy[1−5] have given unprecedented information about the dynamical behavior of large single polymer molecules in solution, in particular the small-scale kinetics of individual monomers inaccessible to traditional techniques like dynamic light scattering. One of the first studies along this direction yielded an unexpected result. Shusterman et al.[2] observed the random motion of a single labeled monomer at the end of a long double-stranded DNA molecule and found evidence of an "intermediate Rouse regime": the mean-squared displacement (MSD) followed a scaling $\langle r^2(t)\rangle \propto t^{1/2}$ for a wide time range corresponding to polymer motion at length scales smaller than the chain length L but larger than the persistence length l_p. This agrees with the free-draining Rouse model for a polymer which neglects hydrodynamic interactions mediated by flow fields arising from the monomers moving through the solvent. Such a result contradicts the conventional wisdom for flexible polymers, which states that these hydrodynamic interactions play a crucial role in polymer dynamics in dilute solutions and give rise to nondraining behavior that is qualitatively described by the Zimm theory, which predicts $\langle r^2(t)\rangle \propto t^{2/3}$.[6,7] Though double-stranded DNA is a semiflexible polymer (having a persistence length $l_p \approx 50-100$ nm much larger than the width $\approx$2 nm), the expectation for kinetics at scales larger than l_p is that it behaves like a nondraining flexible polymer. Thus, the apparent absence of hydrodynamic effects is quite surprising, and the intermediate Rouse regime does not fit into established theories of the dynamics of *flexible* polymers in dilute solutions, though recently there has been an attempt to explain its existence through a theory exhibiting time-dependent hydrodynamic screening.[8] On the other hand, a new experimental study by Petrov et al.[5] on the same system did not seem to show the Rouse regime, and its results were interpreted to be generally consistent with the dynamics predicted by the Zimm theory. Arguably the dynamics of a semiflexible polymer such as DNA may be expected to differ from that of flexible polymers. However, with the exception of the Harnau, Winkler, Reineker (HWR) model,[9] other established theories of the dynamics of semiflexible polymers[10,11] treat only the range of displacements smaller than the persistence length $\langle r^2(t)\rangle < l_p^2$.

To help resolve the controversy over the dynamics of semiflexible polymers on intermediate length scales $l_p^2 < \langle r^2(t)\rangle < L^2$, we study the end-monomer behavior of semiflexible chains in dilute solutions using two approaches: dynamic mean-field theory (MFT) that includes hydrodynamics with the preaveraging approximation and Brownian hydrodynamics simulations without the preaveraging approximation. The end-monomer MSD, diffusion constants, and longest relaxation times from the two approaches agree closely with each other. While the hydrodynamic preaveraging MFT method is similar to that of HWR in ref 9, we have improved the approximation by taking into account the full hydrodynamic interaction matrix in the Langevin equation and not just the diagonal contribution. This leads to much better agreement between the MFT and the simulation data: compared with the earlier version, the improved MFT is 10−65% closer to the mean-square displacement $\langle r^2(t)\rangle$ of the end monomer obtained by simulations for time scales shorter than the longest relaxation time of the chain and reduces the discrepancy in the effective local exponent $\alpha(t) = \mathrm{d}(\log\langle r^2(t)\rangle)/\mathrm{d}(\log t)$ in this time range, which is underestimated by as much as 10% using the earlier method. Thus, we can confidently extend the MFT to larger chain lengths L that are inaccessible to simulation. For these chains we find an intermediate dynamical regime where the continuously varying effective local exponent of the end-monomer MSD, $\alpha(t)$, drops below 2/3, and its difference from this Zimm value increases with L. The

* To whom correspondence should be addressed.
† TÜBITAK - Bosphorus University.
‡ Technical University of Munich.
§ University of North Carolina.
⊥ Ben-Gurion University.

10.1021/ma802017g CCC: $40.75 © 2009 American Chemical Society
Published on Web 01/15/2009

existence of this regime and the qualitative trends of $\alpha(t)$ with changing L and l_p are verified independently through a heuristic scaling argument. However, even at the largest chain lengths examined, comparable to or longer than the experimentally studied chains of refs 2 and 5, the effective exponent $\alpha(t)$ does not reach the Rouse limit of 1/2. Comparison with the experimental MSD data of ref 2 reveals two interesting results: the MFT accurately describes the long-time diffusion behavior, related to the large-scale dynamics of the chain; however, at shorter times it underestimates the extent of the MSD. As we show in this paper, the same sub-Zimm scaling of the MSD is also contained in the HWR theory that was used to successfully fit the data of ref 5. So the question is not whether an intermediate sub-Zimm scaling regime exists, but rather how large that regime is and how small are the intermediate exponents. The remaining discrepancy between theory and experiment discussed in this paper highlights the importance of additional dynamical degrees of freedom absent in the wormlike chain model used as the starting point for the theoretical description of DNA or some shortcomings in the current analysis of FCS data.

The paper is organized as follows: in section 2 we give a heuristic scaling argument that captures the basic properties of the intermediate dynamical regime; in section 3 we describe the details of the Brownian dynamics simulations; in section 4 we give an overview of the mean-field model for semiflexible polymers and the preaveraging approximation used to determine its behavior in solution; in section 5 we compare the simulation, MFT, and heuristic results, together with the experimental data. The dynamical regimes exhibited in these results are examined through asymptotic scaling analysis in section 6 and placed in the context of earlier theories. Finally, section 7 summarizes the main points of the paper. Additional material, extending the mean-field model of section 4 to extensible wormlike chains, is provided in Appendix A. Mathematical details of an analytical approximation used in section 6 are given in Appendix B.

2. Heuristic Scaling Argument

Certain qualitative features of the intermediate dynamical regime for semiflexible polymers can be derived from a scaling argument similar to the one that is typically used to understand subdiffusive motion in the Rouse or Zimm models.[12] In our heuristic scaling, we assume that at time scales t the diffusion of the polymer is characterized by the coherent motion of a section with contour length $\ell(t)$. The MSD of a monomer during this time t has two limiting subdiffusive behaviors depending on the magnitude of $\ell(t)$. For $\ell(t) \ll l_p$, where the local stiffness of the polymer plays the key role, the MSD $\langle r^2(t)\rangle$ is dominated by transverse chain fluctuations, and thus $\langle r^2(t)\rangle \sim \ell(t)^3/l_p$.[10−15] For $\ell(t) \gg l_p$, the MSD can be estimated as $\langle r^2(t)\rangle \sim r_{ee}^2(\ell(t))$, where $r_{ee}^2(\ell)$ is the mean-squared end-to-end distance of a polymer of contour length ℓ. For a semiflexible chain with persistence length l_p this is given by

$$r_{ee}^2(\ell) = 2l_p\ell - 2\ell_p^2(1 - e^{-\ell/l_p}) \tag{1}$$

Thus, the total intramolecular contribution to the MSD, $\langle r_{intra}^2(t)\rangle$, can be written in a heuristic form which smoothly interpolates between these two limits:

$$\langle r_{intra}^2(t)\rangle = C_1\left[\{r_{ee}^2(\ell(t))\}^{-\phi_1} + C_1'\left\{\frac{(r_{ee}^2(\ell(t)))^{3/2}}{l_p}\right\}^{-\phi_1}\right]^{-1/\phi_1} \tag{2}$$

Using the fact that $r_{ee}^2(\ell) \approx \ell^2$ for $\ell \ll l_p$, one can easily check that eq 2 has the appropriate asymptotic limits for small and large $\ell(t)$, with the crossover occurring at $t \approx \tau_p$ where the relaxation time τ_p of a persistent segment is defined by $r_{ee}^2(\ell(\tau_p)) = l_p^2$. We added numerical constants $C_1, C_1' \sim O(1)$, and a crossover exponent ϕ_1 which will be determined from the comparison with numerical data.

In order to close the scaling argument, we write the diffusion relation between spatial and temporal scales

$$\langle r_{intra}^2(t)\rangle = 6D(\ell(t))t \tag{3}$$

in terms of an effective diffusion constant $D(\ell)$ for a polymer section of length ℓ. $D(\ell)$ can be estimated from a heuristic formula[16] that compares well with both simulation and experimental DNA results:

$$D(\ell) = C_2(D_{cyl}^{\phi_2}(\ell) + D_{coil}^{\phi_2}(\ell))^{1/\phi_2} \tag{4}$$

where

$$D_{cyl}(l) = \frac{2\mu_0 k_B T a}{l}\left[\log\frac{l}{2a} + 0.312 + 0.565\left(\frac{2a}{l}\right) - 0.1\left(\frac{2a}{l}\right)^2\right]$$
$$D_{coil}(l) = \frac{2.22\mu_0 k_B T a}{\sqrt{l_p l}} \tag{5}$$

Here $2a$ is the diameter of the chain, $\mu_0 = 1/(6\pi\eta a)$ is the Stokes mobility of a single sphere of radius a, and η is the viscosity of water. $D_{cyl}(\ell)$ is the diffusion constant of a stiff cylinder,[17] and $D_{coil}(\ell)$ gives the diffusion constant of an ideal chain in the flexible limit where $\ell \gg l_p$. We assume $\ell \ll l_p^3/a^2$, so self-avoidance effects can be ignored.[18] For parameter values $a =$ 1 nm and $l_p = 50$ nm, typical of DNA, these effects are only important at scales greater than $\sim 10^2$ μm, far larger than the chain lengths investigated in the experimental studies discussed above. Equation 4 is an interpolation between the limiting cases given by $D_{cyl}(\ell)$ when $\ell \ll l_p$ and $D_{coil}(\ell)$ when $\ell \gg l_p$. In ref 16 the crossover exponent was determined to be $\phi_2 = 3$, and with the definition of $D_{cyl}(\ell)$ and $D_{coil}(\ell)$ the constant was fixed at $C_2 = 1$. In the present context we use ϕ_2 and $C_2 \sim O(1)$ as parameters that will be adjusted to fit the numerical data.

The asymptotic Zimm scaling is easily obtained from the expressions written so far: In the flexible regime, for $\ell \gg l_p$, we have $D \sim (\ell/l_p)^{-1/2}$, and from eqs 1 and 2, we find $\langle r_{intra}^2\rangle \sim \ell l_p$. Using $\langle r_{intra}^2\rangle \sim Dt$ from eq 3, we thus obtain $\ell \sim t^{2/3}/l_p$ and $\langle r_{intra}^2\rangle \sim t^{2/3}$, the well-known Zimm scaling for flexible polymers.[12] In the stiff polymer regime, for $\ell \ll l_p$, we have $D \sim \ell^{-1}\log(\ell/a)$, and from eq 2 we find $\langle r_{intra}^2\rangle \sim \ell^3/l_p$. Again using $\langle r_{intra}^2\rangle \sim Dt$, we obtain this time $\ell \sim (tl_p \log t)^{1/4}$ and thus $\langle r_{intra}^2\rangle \sim t^{3/4}l_p^{-1/4}\log^{3/4} t$. The MSD scaling of semiflexible polymers has pronounced logarithmic corrections in the stiff polymer regime due to hydrodynamic effects.

To get an expression for the total MSD, $\langle r^2(t)\rangle$, that includes the long-time regime, one must consider also the crossover which occurs near time $t = \tau$, where $\ell(\tau) = L$, the total contour length of the chain. For $t \gg \tau$ the effective diffusion constant is $D(L)$, and $\langle r^2(t)\rangle \approx 6D(L)t$, describing the trivial diffusion of the whole polymer coil. τ corresponds approximately to the longest relaxation time of the polymer. This crossover is captured by yet another crossover expression

$$\langle r^2(t)\rangle = [\langle r_{intra}^2(t)\rangle^{\phi_3} + \{6D(L)t\}^{\phi_3}]^{1/\phi_3} \tag{6}$$

which gives the correct asymptotic scaling behavior for $\langle r^2(t)\rangle$ at all time regimes. In the results below, the exponents ϕ_1, ϕ_2, ϕ_3, and the three constants C_1, C_1', C_2 in eqs 2, 4, and 6 are chosen so that the heuristic scaling argument approximately agrees, for long chain lengths, with the numerical results of the MFT approach described in the next section. The best-fit values

are $\phi_1 = 0.84$, $\phi_2 = 3.15$, $\phi_3 = 3.62$, $C_1 = 3.65$, $C_1' = 0.66$, and $C_2 = 1.31$.

The full time dependence covering also the nonasymptotic behavior is obtained by equating the expressions for $\langle r^2_{\text{intra}}(t)\rangle$ in eqs 2 and 3 and implicitly solving for $\ell(t)$; we thus calculate $\langle r^2_{\text{intra}}(t)\rangle$ as a function of t. Plugging the result for $\langle r^2_{\text{intra}}(t)\rangle$ into eq 6 gives the total MSD $\langle r^2(t)\rangle$. The time evolution of $\langle r^2(t)\rangle$ can be expressed through the effective exponent $\alpha(t) = \mathrm{d}(\log\langle r^2(t)\rangle)/\mathrm{d}(\log t)$. Figure 1a shows $\alpha(t)$ vs t/τ for chains of total length $L = 12000a$, with various persistence lengths in the range $l_p = 50a-4000a$. The dot along each $\alpha(t)$ curve marks $\alpha(\tau_p)$. There is clearly an intermediate time regime, within the range $\tau_p < t < \tau$, where $\alpha(t)$ dips below the Zimm value of 2/3 (for $l_p < 1800a$). The minimum value of $\alpha(t)$ over all t depends both on L and l_p, as shown in Figure 1b,c, which plot $\min_t \alpha$ vs l_p/L for several chain lengths $L = 200a-12000a$ and $\min_t \alpha$ vs L/l_p for several l_p in the range $l_p = 50a-1800a$. The overall variation of $\min_t \alpha$ as a function of L/a and l_p/a is depicted in the contour diagram of Figure 2. The deviation from Zimm behavior becomes more prominent with increasing L: the time range where $\alpha < 2/3$ increases and the values of $\min_t \alpha$ decrease. As seen in Figure 1c, for fixed l_p/a the decrease in $\min_t \alpha$ with L eventually saturates for $L \gg l_p$. The $\min_t \alpha$ curves in Figure 1b all reach a minimum in the range $l_p/L \sim 0.01-0.04$. The position of the minimum decreases with L approximately with the logarithmic dependence $l_p/L \approx -0.013 + 0.26/\log(L/a)$. The exponent values at these minima, $\min_{l_p} \min_t \alpha$, also have a nearly linear dependence on $1/\log(L/a)$, as can be seen in Figure 1d, where $\min_{l_p} \min_t \alpha$ goes from 0.677 at $L = 200a$ to 0.591 at $L = 12000a$. The best-fit line is $\min_{l_p} \min_t \alpha \approx 0.48 + 1.04/\log(L/a)$. (If data from L much larger than the experimental range are also included, the $L = \infty$ extrapolation of $\min_{l_p} \min_t \alpha$ shifts from 0.48, approaching 1/2.) The growing deviation from Zimm behavior with L is possibly related to the observation in ref 2 that the intermediate Rouse regime becomes more noticeable at longer coil sizes, occupying a larger range of times. However, in contrast to ref 2, the exponent α never reaches the true Rouse value of 1/2 even at the longest realistic chain lengths. For $l_p = 50a$, corresponding to the DNA persistence length, $\min_t \alpha$ at $L = 12000a$ is 0.602.

The origin of this intermediate regime where $\alpha(t) < 2/3$ can be linked to the crossover behaviors of $\langle r^2_{\text{intra}}\rangle$ and $D(\ell)$. Assume ℓ is in the range $l_p < \ell < L$ and is sufficiently large that $\langle r^2_{\text{intra}}\rangle \sim \ell l_p$ but small enough that $D(\ell)$ has not reached the asymptotic limit $D_{\text{coil}}(\ell) \sim (\ell l_p)^{-1/2}$. Since the total MSD $\langle r^2\rangle \sim \langle r^2_{\text{intra}}\rangle$ in this regime, one can use $\langle r^2_{\text{intra}}\rangle \sim Dt$ and $\langle r^2_{\text{intra}}\rangle \sim \ell l_p$ to relate the effective exponent $\alpha = \mathrm{d}(\log\langle r^2\rangle)/\mathrm{d}(\log t)$ to $D(\ell)$, giving $\alpha = (1 - (\ell/D)\partial D/\partial \ell)^{-1}$. As $D(\ell)$ is in the crossover region between $D_{\text{cyl}}(\ell)$ and $D_{\text{coil}}(\ell)$, it must decrease with ℓ slower than $\ell^{-1}\log(\ell/a)$ but faster than $\ell^{-1/2}$. These two limits mean that α is bounded by $1/(2 - \log^{-1}(\ell/a)) > 1/2$ from below, and 2/3 from above, corresponding precisely to the intermediate dynamical regime.

The existence of this regime will be confirmed through the Brownian dynamics and MFT calculations described in the next two sections. In section 5 we will see that the qualitative trends illustrated in Figure 1a−d agree very well with the results from the more sophisticated MFT approach and thus allow for a simple explanation of sub-Zimm scaling behavior in terms of hydrodynamic effects on the diffusion behavior of a semiflexible polymer in the crossover between two limiting regimes.

3. Brownian Dynamics Simulation

For the numerical Brownian dynamics simulations[19,20] we model the polymer as a connected chain of M spheres, each having radius a and position $r_i(t)$, $i = 1,\ldots, M$. The sphere positions evolve in time according to the Langevin equation

$$\frac{\mathrm{d}\mathbf{r}_i(t)}{\mathrm{d}t} = \sum_{j=1}^{M} \vec{\boldsymbol{\mu}}_{ij} \cdot \left(-\frac{\partial U(\mathbf{r}_1, \ldots, \mathbf{r}_M)}{\partial \mathbf{r}_j}\right) + \boldsymbol{\xi}_i(t) \qquad (7)$$

appropriate for the low Reynolds number regime. Here $\vec{\boldsymbol{\mu}}_{ij}$ is the Rotne−Prager tensor[21] describing hydrodynamic interactions between the monomers

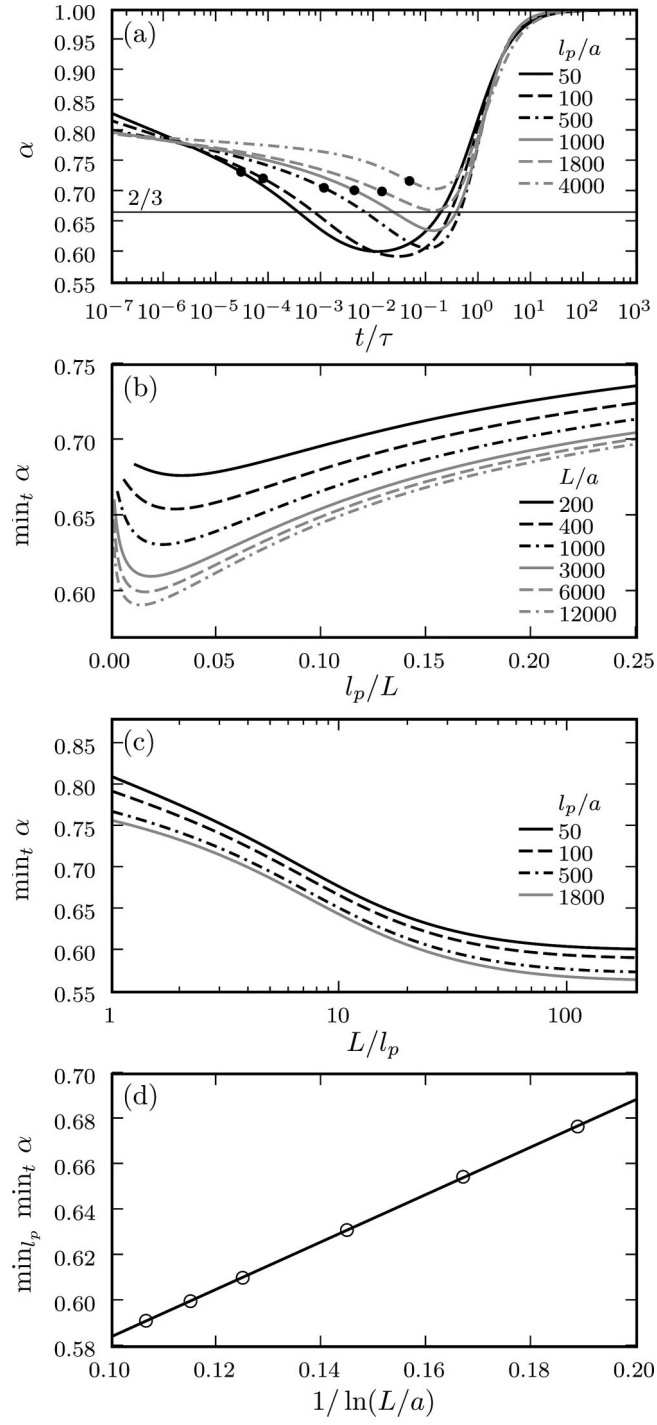

Figure 1. Results of the heuristic scaling argument described in section 2. (a) The effective exponent $\alpha = \mathrm{d}(\log\langle r^2(t)\rangle)/\mathrm{d}(\log t)$ vs t/τ for polymers of diameter $2a$, contour length $L = 12000a$, and various persistence lengths $l_p = 50a-4000a$. The dot along each $\alpha(t)$ curve marks $\alpha(\tau_p)$. The time scales τ and τ_p are defined in the text. (b) The minimum value of α over all t vs l_p/L for several $L = 200a-12000a$. (c) The minimum value of α over all t vs L/l_p for several $l_p = 50a-1800a$. (d) The circles show the minimum value of α in each of the curves in panel (b), plotted as a function of $1/\ln(L/a)$. Superimposed is a straight-line fit to the data points, $\min_{l_p} \min_t \alpha \approx 0.48 + 1.04/\ln(L/a)$.

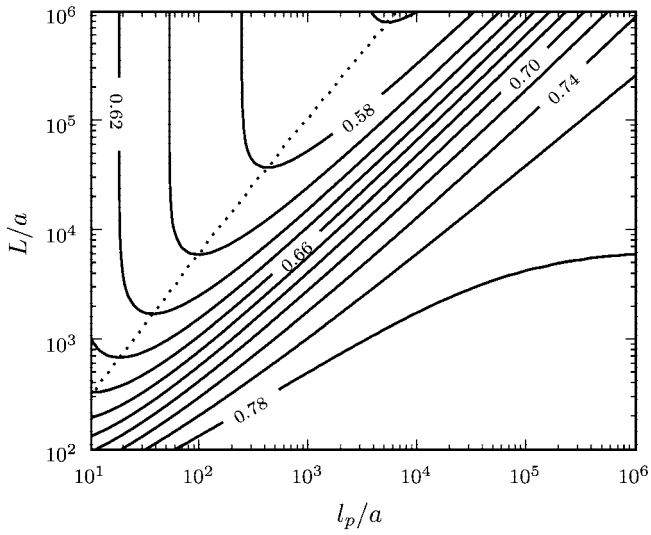

Figure 2. Contours show the minimum value of the effective exponent $\alpha(t) = d(\log\langle r^2(t)\rangle)/d(\log t)$ over all t calculated using the heuristic scaling argument in section 2 for chains of diameter $2a$, total length L, and persistence length l_p. The interval between contours is 0.02. The dotted line indicates the minimum value of $\min_t \alpha$ over l_p/a for a given L/a.

$$\overleftrightarrow{\boldsymbol{\mu}}_{ij} = \mu_0\delta_{i,j}\overleftrightarrow{\mathbf{1}} + (1-\delta_{i,j})\left(\frac{1}{8\pi\eta r_{ij}}\left[\overleftrightarrow{\mathbf{1}} + \frac{\mathbf{r}_{ij}\otimes\mathbf{r}_{ij}}{r_{ij}^2}\right] + \frac{a^2}{4\pi\eta r_{ij}^3}\left[\frac{\overleftrightarrow{\mathbf{1}}}{3} - \frac{\mathbf{r}_{ij}\otimes\mathbf{r}_{ij}}{r_{ij}^2}\right]\right) \quad (8)$$

where $\mathbf{r}_{ij} \equiv \mathbf{r}_i - \mathbf{r}_j$, and $\overleftrightarrow{\mathbf{1}}$ is the 3×3 identity matrix. The stochastic velocity $\boldsymbol{\xi}_i(t)$ in eq 7 is Gaussian, with correlations given by the fluctuation−dissipation equation:

$$\langle \boldsymbol{\xi}_i(t) \otimes \boldsymbol{\xi}_j(t')\rangle = 2k_BT\,\overleftrightarrow{\boldsymbol{\mu}}_{ij}\delta(t-t') \quad (9)$$

The final component of the model is the elastic potential $U(\mathbf{r}_1,..., \mathbf{r}_M)$ in eq 7, depending on the positions of the spheres. This potential consists of two parts

$$U = U_{WLC} + U_{LJ} \quad (10)$$

with

$$U_{WLC} = \frac{\gamma}{4a}\sum_{i=1}^{M-1}(r_{i+1,i} - 2a)^2 + \frac{\epsilon}{2a}\sum_{i=2}^{M-1}(1-\cos\theta_i)$$
$$U_{LJ} = \omega\sum_{i<j}\Theta(2a - r_{ij})\left[\left(\frac{2a}{r_{ij}}\right)^{12} - 2\left(\frac{2a}{r_{ij}}\right)^6 + 1\right] \quad (11)$$

Here θ_i is the angle between $\mathbf{r}_{i+1,i}$ and $\mathbf{r}_{i,i-1}$. The U_{WLC} term describes the stretching and bending forces associated with the extensible wormlike chain model, with stretching modulus γ and bending modulus ϵ. The latter is related to the persistence length l_p of the polymer through $\epsilon = l_pk_BT$. For all the simulations the stretching modulus is set at $\gamma = 200k_BT/a$, which is large enough that the total contour length of the polymer stays approximately constant. The U_{LJ} term is a truncated Lennard-Jones interaction with strength $\omega = 3k_BT$.

To implement eq 7 numerically, we discretize it with time step τ and use nondimensionalized variables, measuring lengths in units of a, times in units of $a^2/(k_BT\mu_0)$, and energies in units of k_BT. For a given contour length $L = 2aM$ and persistence length l_p, the results described below are based on averages taken from 15 to 50 independent runs, each with time step $\tau = 3 \times 10^{-4}a^2/(k_BT\mu_0)$ and lasting for $\sim 10^8-10^9$ steps. The first 10^6 steps of a run are not used for data collection, and afterward output data are collected every 10^3-10^4 steps.

4. Mean-Field Model of Polymer Dynamics

The derivation of the mean-field model for semiflexible polymers is described below. Readers not interested in the technical details may skip this section, the main result of which is eq 37 for the end-monomer MSD in terms of several parameters: the diffusion constant D, relaxation times τ_n, and coefficients Δ_n. All of these parameters can be determined for a given L and l_p by obtaining the normal modes and numerically evaluating the hydrodynamic interaction matrix H as outlined in eqs 30−34.

The analytical model of the polymer is a continuous space curve $\mathbf{r}(s)$ of total length L, with contour coordinate s in the range $-L/2 \le s \le L/2$. The simplest expression for the elastic energy U of the chain, incorporating the effects of rigidity, is that of Kratky and Porod[22]

$$U = \frac{\epsilon}{2}\int ds\left(\frac{\partial\mathbf{u}(s)}{\partial s}\right)^2 \quad (12)$$

where ϵ is the bending modulus introduced above, $\epsilon = l_pk_BT$, and the tangent vector $\mathbf{u} \equiv \partial\mathbf{r}/\partial s$ is subject to the constraint $\mathbf{u}^2(s) = 1$ at each s. As in section 2, we assume $L \ll l_p^3/a^2$, so we ignore self-avoidance effects. The associated free energy is $F = -\beta^{-1}\log Z$, with $\beta^{-1} \equiv k_BT$ and the partition function Z given by the functional integral

$$Z = \int \mathscr{D}\mathbf{u}\prod_s \delta(\mathbf{u}^2(s) - 1)e^{-\beta U} \quad (13)$$

The delta function enforcing the constraint can be equivalently written using an additional functional integral over a complex auxiliary field $\lambda(s)$

$$Z = \int_{-i\infty}^{i\infty}\mathscr{D}\lambda\int\mathscr{D}\mathbf{u}e^{-\beta U - \beta\int ds\lambda(s)(\mathbf{u}^2(s)-1)}$$
$$\equiv \int_{-i\infty}^{i\infty}\mathscr{D}\lambda e^{-\beta\mathscr{F}[\lambda]} \quad (14)$$

where we introduce the functional $\mathscr{F}[\lambda]$ and ignore any constants arising from the normalization of the integral. Since calculations with this partition function are generally intractable due to the tangent vector constraint, we employ the mean-field theory (MFT) approach developed by Ha and Thirumalai,[23,24] evaluating the functional integral over $\lambda(s)$ using a stationary-phase approximation:

$$Z = \int_{-i\infty}^{i\infty}\mathscr{D}\lambda e^{-\beta\mathscr{F}[\lambda]} \approx e^{-\beta\mathscr{F}[\lambda_{cl}]} \quad (15)$$

Here $\lambda_{cl}(s)$ is the path satisfying the stationary-phase condition $\delta\mathscr{F}/\delta\lambda(s) = 0$, and we have neglected higher-order correction terms. The resulting MFT free energy $F_{MF} \equiv \mathscr{F}[\lambda_{cl}]$ takes the form[23]

$$F_{MF} = -\beta^{-1}\log\int\mathscr{D}\mathbf{u}e^{-\beta U_{MF}} \quad (16)$$

where

$$U_{MF} = \frac{\epsilon}{2}\int ds\left(\frac{\partial\mathbf{u}(s)}{\partial s}\right)^2 + \nu\int ds\,\mathbf{u}^2(s) + \nu_0(\mathbf{u}^2(L/2) + \mathbf{u}^2(-L/2)) \quad (17)$$

and the constants ϵ, ν, and ν_0 are related by

$$\sqrt{\frac{\nu\epsilon}{2}} = \nu_0 = \frac{3}{4}k_BT \tag{18}$$

Comparing the results of this mean-field analytical model to those of the simulation described in the last section, we note that the simulation potential energy in eqs 10 and 11 contains an additional extensional term with large parameter $\gamma \gg k_BT/a$. Applying the mean-field approach to an extensible wormlike chain leads to a value of the effective stretching moduli ν and ν_0 slightly modified from that of eq 18, with corrections of the order of ϵ/Γ, where $\Gamma = 4a^2\gamma$. The details are described in Appendix A. Assuming ϵ and Γ are fixed in the continuum limit, and $\Gamma \gg \epsilon$, one can ignore the finite extensibility of the chain in constructing the mean-field theory.

The MFT elastic energy of eq 17 can be derived in several alternative ways: it was first proposed by Lagowski, Noolandi, and Nickel[25] as a modification of the Harris−Hearst model[26] that corrected chain inhomogeneities due to end fluctuations; it was later independently derived from the maximum entropy principle by Winkler, Reineker, and Harnau.[27] The main consequence of the approximation is that the local constraint $\mathbf{u}^2(s) = 1$ is relaxed and replaced by the condition $\langle \mathbf{u}^2(s) \rangle = 1$. If the relationship between the bending modulus ϵ and l_p is redefined as $\epsilon = (3/2)l_pk_BT$ in U_{MF}, the tangent vector correlation function has the same form as in the Kratky−Porod chain

$$\langle \mathbf{u}(s)\cdot\mathbf{u}(s') \rangle = \exp(-|s' - s|/l_p) \tag{19}$$

Related quantities like the mean-squared end-to-end distance and radius of gyration are also correctly reproduced by the MFT approximation with this redefinition of ϵ, and thus we will use it for the remainder of the paper. This applies only to the MFT elastic energy of eq 17; in the simulation U_{WLC} of eq 10 ϵ retains its original definition.

In deriving the diffusion behavior of the polymer in solution, we follow an approach similar to that of HWR,[9] who first studied the dynamical characteristics of the MFT model given by eq 17 using a hydrodynamic preaveraging approximation along the lines of the Zimm model.[6,7] To describe the time evolution of the chain $\mathbf{r}(s, t)$ in the presence of hydrodynamic interactions, we start with the Langevin equation:

$$\frac{\partial}{\partial t}\mathbf{r}(s,t) = -\int_{-L/2}^{L/2} ds' \overleftrightarrow{\boldsymbol{\mu}}(s,s';\mathbf{r}(s,t) - \mathbf{r}(s',t))\frac{\delta U_{MF}}{\delta \mathbf{r}(s',t)} + \boldsymbol{\xi}(s,t) \tag{20}$$

Here the $\boldsymbol{\xi}(s,t)$ is the stochastic contribution, and $\overleftrightarrow{\boldsymbol{\mu}}(s, s'; \mathbf{x})$ is the continuum version of the Rotne−Prager tensor in eq 8[9]

$$\overleftrightarrow{\boldsymbol{\mu}}(s,s';\mathbf{x}) = 2a\mu_0\delta(s - s')\overleftrightarrow{\mathbf{1}} + \Theta(x - 2a) \times \left(\frac{1}{8\pi\eta x}\left[\overleftrightarrow{\mathbf{1}} + \frac{\mathbf{x}\otimes\mathbf{x}}{x^2}\right] + \frac{a^2}{4\pi\eta x^3}\left[\frac{\overleftrightarrow{\mathbf{1}}}{3} - \frac{\mathbf{x}\otimes\mathbf{x}}{x^2}\right]\right) \tag{21}$$

with the Θ function excluding unphysical configurations.

The preaveraging approximation consists of replacing $\overleftrightarrow{\boldsymbol{\mu}}(s, s'; \mathbf{r}(s, t) - \mathbf{r}(s', t))$ in eq 20, which involves a complicated dependence on the specific chain configuration at time t, with an average over all equilibrium configurations, $\overleftrightarrow{\boldsymbol{\mu}}_{avg}(s,s')$, that depends only on the contour coordinates s and s'. This tensor $\overleftrightarrow{\boldsymbol{\mu}}_{avg}$ is defined as

$$\overleftrightarrow{\boldsymbol{\mu}}_{avg}(s,s') = \int d^3\mathbf{x}\overleftrightarrow{\boldsymbol{\mu}}(s,s';\mathbf{x})G(s,s';\mathbf{x}) \tag{22}$$

where $G(s, s'; \mathbf{x})$ is the equilibrium probability of finding two points at s and s' along the polymer contour whose spatial positions differ by the vector $\mathbf{x}$. For the MFT model of eq 17, this probability is[27]

$$G(s,s';\mathbf{x}) = \left(\frac{3}{2\pi\sigma(|s - s'|)}\right)^{3/2}\exp\left(-\frac{3x^2}{2\sigma(|s - s'|)}\right) \tag{23}$$

where $\sigma(l) \equiv 2l_pl - 2l_p^2(1 - \exp(-l/l_p))$, the mean-squared end-to-end distance of a chain of length l. Plugging eq 23 into eq 22, we find

$$\overleftrightarrow{\boldsymbol{\mu}}_{avg}(s,s') = \left[2a\mu_0\delta(s - s') + \frac{\Theta(|s - s'| - 2a)}{\eta\sqrt{6\pi^3\sigma(|s - s'|)}} \times \exp\left(-\frac{6a^2}{\sigma(|s - s'|)}\right)\right]\overleftrightarrow{\mathbf{1}} \equiv \mu_{avg}(s - s')\overleftrightarrow{\mathbf{1}} \tag{24}$$

For the same reason as in eq 21, we have added a Θ function to the final result.

The preaveraged version of the Langevin equation is thus

$$\frac{\partial}{\partial t}\mathbf{r}(s,t) = \int_{-L/2}^{L/2} ds'\mu_{avg}(s - s')\left(-\frac{\delta U_{MF}}{\delta \mathbf{r}(s',t)}\right) + \boldsymbol{\xi}(s,t) \tag{25}$$

We assume the $\boldsymbol{\xi}(s, t)$ are Gaussian random vectors, whose components $\xi^{(i)}(s,t)$ have correlations given by the fluctuation−dissipation theorem:

$$\langle \xi^{(i)}(s,t)\xi^{(j)}(s',t') \rangle = 2k_BT\delta_{ij}\delta(t - t')\mu_{avg}(s - s') \tag{26}$$

Using U_{MF} from eq 17, the force term in eq 25 can be written as

$$-\frac{\delta U_{MF}}{\delta \mathbf{r}(s',t)} = -\epsilon\frac{\partial^4}{\partial s^4}\mathbf{r}(s',t) + 2\nu\frac{\partial^2}{\partial s^2}\mathbf{r}(s',t) \tag{27}$$

with free-end boundary conditions at $s = \pm L/2$ of the form

$$\epsilon\frac{\partial^3}{\partial s^3}\mathbf{r}(\pm L/2,t) - 2\nu\frac{\partial}{\partial s}\mathbf{r}(\pm L/2,t) = 0$$
$$\mp\epsilon\frac{\partial^2}{\partial s^2}\mathbf{r}(\pm L/2,t) - 2\nu_0\frac{\partial}{\partial s}\mathbf{r}(\pm L/2,t) = 0 \tag{28}$$

To rewrite the Langevin equation in matrix form, we assume $\boldsymbol{\xi}(s,t)$ satisfies similar boundary conditions to $\mathbf{r}(s,t)$ and expand both $\mathbf{r}(s,t)$ and $\boldsymbol{\xi}(s,t)$ in normal modes $\psi_n(s)$, with amplitudes $\mathbf{p}_n(t)$ and $\mathbf{q}_n(t)$, respectively:

$$\mathbf{r}(s,t) = \sum_{n=0}^{\infty}\mathbf{p}_n(t)\psi_n(s), \quad \boldsymbol{\xi}(s,t) = \sum_{n=0}^{\infty}\mathbf{q}_n(t)\psi_n(s) \tag{29}$$

We choose the normal modes $\psi_n(s)$ to be eigenfunctions of the differential operator in eq 27, satisfying

$$\epsilon\frac{\partial^4}{\partial s^4}\psi_n(s) - 2\nu\frac{\partial^2}{\partial s^2}\psi_n(s) = \lambda_n\psi_n(s) \tag{30}$$

for eigenvalues λ_n. These $\psi_n(s)$ take the form[9]

$$\psi_0(s) = \sqrt{\frac{1}{L}}$$

$$\psi_n(s) = \sqrt{\frac{A_n}{L}}\left(\alpha_n\frac{\sin\alpha_ns}{\cos\alpha_nL/2} + \beta_n\frac{\sinh\beta_ns}{\cosh\beta_nL/2}\right), \quad n \text{ odd}$$

$$\psi_n(s) = \sqrt{\frac{A_n}{L}}\left(-\alpha_n \frac{\cos \alpha_n s}{\sin \alpha_n L/2} + \beta_n \frac{\cosh \beta_n s}{\sinh \beta_n L/2}\right), \quad n \text{ even} \tag{31}$$

with

$$\beta_n^2 - \alpha_n^2 = 2\nu/\epsilon, \quad \lambda_0 = 0, \quad \lambda_n = \epsilon\alpha_n^4 + 2\nu\alpha_n^2 \tag{32}$$

The constants α_n and β_n can be determined from the boundary conditions in eq 28, while the A_n are normalization coefficients. Using eqs 29, 30, and the orthonormality of the ψ_n, eqs 25 and 26 become

$$\frac{\partial}{\partial t}\mathbf{p}_n(t) = -\sum_{m=0}^{\infty} H_{nm}\lambda_m \mathbf{p}_m(t) + \mathbf{q}_n(t)$$
$$\langle q_{ni}(t) q_{mj}(t')\rangle = 2k_B T \delta_{ij}\delta(t - t')H_{nm} \tag{33}$$

where

$$H_{nm} = \int_{-L/2}^{L/2} \mathrm{d}s \int_{-L/2}^{L/2} \mathrm{d}s' \psi_n(s)\mu_{\mathrm{avg}}(s - s')\psi_m(s') \tag{34}$$

The matrix elements H_{nm} can be evaluated through numerical integration. HWR neglect the off-diagonal portion of this interaction matrix H, since the diagonal elements typically dominate. However, as we will show later, this approximation leads to an inaccurate description of the simulation results for the end-monomer dynamics at short times, demonstrating that the off-diagonal elements are negligible only at times longer than the bending relaxation time. A more accurate approach is to take the whole matrix H, keep only the leading $N \times N$ sub-block (describing the interactions among the N slowest-relaxing modes), and exactly solve the resulting finite-dimensional version of eq 33. An appropriate value for N can be estimated as follows. For the oscillation described by mode $\psi_n(s)$ from eq 31, the distance between successive nodes is approximately L/n. The high-frequency cutoff of this distance is on the order of two monomer diameters $4a$, so that only modes with $n \lesssim L/4a$ should be considered. Thus, the natural choice is $N = L/4a$. In the results described in section 5, we use this choice for all chains with $L \leq 1600a$. For longer chains with $L > 1600a$, calculation of the full matrix becomes numerically unfeasible due to roundoff errors in the highly oscillatory integrals of eq 34. Thus, for these chains we truncate N at the maximum value of $N = 400$. This approach gives accurate results at time scales much larger than the relaxation time of the $n = 400$ mode, which is always the case for the time ranges of interest.

To implement this approach, let J be the $N \times N$ matrix with elements $J_{nm} = H_{nm}\lambda_m$, Λ_n the eigenvalues of J, and C the matrix diagonalizing J: $(CJC^{-1})_{nm} = \Lambda_n\delta_{nm}$. Assuming the eigenvalues Λ_n are distinct, and using the fact that H is symmetric, it can also be shown that the matrix C diagonalizes H through the congruent transformation: $(CHC^T)_{nm} = \Theta_n\delta_{nm}$, defining diagonal elements Θ_n.[6] If we introduce a new set of orthogonal functions $\Psi_n(s)$ and the associated amplitudes $\mathbf{P}_n(t)$, $\mathbf{Q}_n(t)$

$$\Psi_n(s) = \sum_{m=0}^{N-1} \psi_m(s)(C^{-1})_{mn}$$

$$\mathbf{P}_n(t) = \sum_{m=0}^{N-1} C_{nm}\mathbf{p}_m(t)$$

$$\mathbf{Q}_n(t) = \sum_{m=0}^{N-1} C_{nm}\mathbf{q}_m(t) \tag{35}$$

then eq 33 becomes

$$\frac{\partial}{\partial t}\mathbf{P}_n(t) = -\Lambda_n \mathbf{P}_n(t) + \mathbf{Q}_n(t)$$
$$\langle Q_{ni}(t) Q_{mj}(t')\rangle = 2k_B T\delta_{ij}\delta(t - t')\Theta_n\delta_{nm} \tag{36}$$

This equation can be solved directly to yield the end-monomer MSD:

$$\langle r^2(t)\rangle \equiv \langle(\mathbf{r}(L/2, t) - \mathbf{r}(L/2, 0))^2\rangle$$
$$= 6Dt + \sum_{n=1}^{N-1} \Delta_n(1 - \mathrm{e}^{-t/\tau_n}) \tag{37}$$

where the diffusion constant $D = k_B T\Theta_0\Psi_0^2(L/2)$, the relaxation times $\tau_n = \Lambda_n^{-1}$, and $\Delta_n = 6k_B T\tau_n\Theta_n\Psi_n^2(L/2)$.

5. Results

The Brownian dynamics simulation and MFT results for the end-monomer and center-of-mass MSD are shown in Figures 3−5 for chain lengths of $L = 100a$, $200a$, and $400a$, respectively, at various persistence lengths l_p. We also show in the bottom panels of each figure the effective local exponent $\alpha(t) = \mathrm{d}\log\langle r^2(t)\rangle/\mathrm{d}\log t$ of the end-monomer MSD curve.

We find in both the simulation and MFT results that $\alpha(t)$ passes through a minimum in the intermediate time range where $l_p^2 < \langle r^2(t)\rangle < r_{ee}^2(L)$. The location of this minimum is on the order of τ_1, the longest relaxation time of the polymer. For $t \gg \tau_1$, as the end-monomer curve approaches the center-of-mass MSD, $\langle r_{c.m.}^2(t)\rangle = 6Dt$, the local slope $\alpha(t)$ tends toward the limiting value of 1. On the other hand, for $t < \tau_p$, where $\langle r^2(t)\rangle < l_p^2$, the stiffness of the polymer dominates, and $\alpha(t)$ varies in the range $\approx 0.8-0.9$. We will discuss both the intermediate and the short-time regimes in more detail below.

There is very good agreement between MFT end-monomer MSD predictions and simulation results in time regimes where simulation results have sufficiently converged to make a comparison. (For $\langle r^2(t)\rangle$ this comparison is possible for nearly the whole simulation time range; for $\alpha(t)$ the numerical uncertainty at the largest times becomes significant and is on the order of the scatter in the plotted data points.) Additionally, dynamical parameters like the diffusion constant D and relaxation time τ_1 determined from the simulation data compare favorably with their MFT values, as shown in Figure 6. The values of D were obtained from the simulations by fitting the center-of-mass MSD data to the straight-line form $\langle r_{c.m.}^2(t)\rangle = 6Dt$. To extract τ_1, the autocorrelation function of the end-to-end vector was calculated, $C_{ee}(t) = \langle \mathbf{r}_{ee}(t)\cdot\mathbf{r}_{ee}(0)\rangle$, where $\mathbf{r}_{ee}(t) = \mathbf{r}_M(t) - \mathbf{r}_1(t)$. For sufficiently large t, this function takes the form of a simple exponential decay, $C_{ee}(t) \sim \exp(-t/\tau_1)$, from which τ_1 can be estimated. For both D and τ_1, only data points for which convergence was achieved were included in the fitting (the criterion for convergence was that the local slope $\mathrm{d}(\log\langle \mathbf{r}_{c.m.}^2(t)\rangle)/\mathrm{d}(\log t) \approx 1$).

The main discrepancies between the two approaches are in the local slopes of the MSD curves at the shortest times, $t \lesssim 10^2 a^2/(k_B T\mu_0)$. This can be explained by the fact that the small-scale motions at short times are particularly sensitive to the discrete nature of the polymer chain and the more strongly fixed monomer−monomer separation in the simulation, thus giving rise to differences with the continuum mean-field approximation. In fact, we can make the MFT mimic the simulation more closely if we exclude the contributions of a fraction of the highest modes in the sum of eq 37, by changing the upper limit from $N - 1$ to $N' - 1$, where $N' = cL/4a$, $0 < c < 1$. A value of $c \approx 1/2$ gives the closest approximation to the simulation MSD and $\alpha(t)$ curves, irrespective of L and l_p. This roughly corresponds to excluding modes where the distance between nodes is shorter than four monomer diameters. The results are

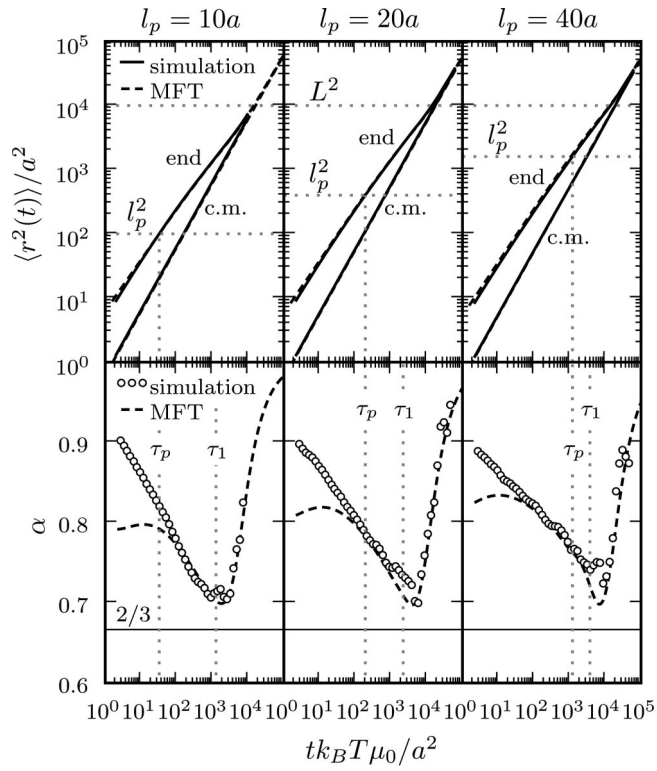

Figure 3. Top panels show simulation and MFT results for the end-monomer and center-of-mass MSD $\langle r^2(t)\rangle/a^2$ for chains of length $L = 100a$ and persistence lengths $l_p = 10a$, $20a$, and $40a$ (a = monomer radius). The bottom panels show the local slope $\alpha = d(\log\langle r^2(t)\rangle)/d(\log t)$ for the end-monomer MSD, with a horizontal line at 2/3 marking the Zimm theory prediction. Two times are indicated by dotted vertical lines: τ_p, the time at which the end-monomer $\langle r^2(\tau_p)\rangle = l_p^2$; and τ_1, the longest relaxation time of the polymer, as determined from the numerical simulations.

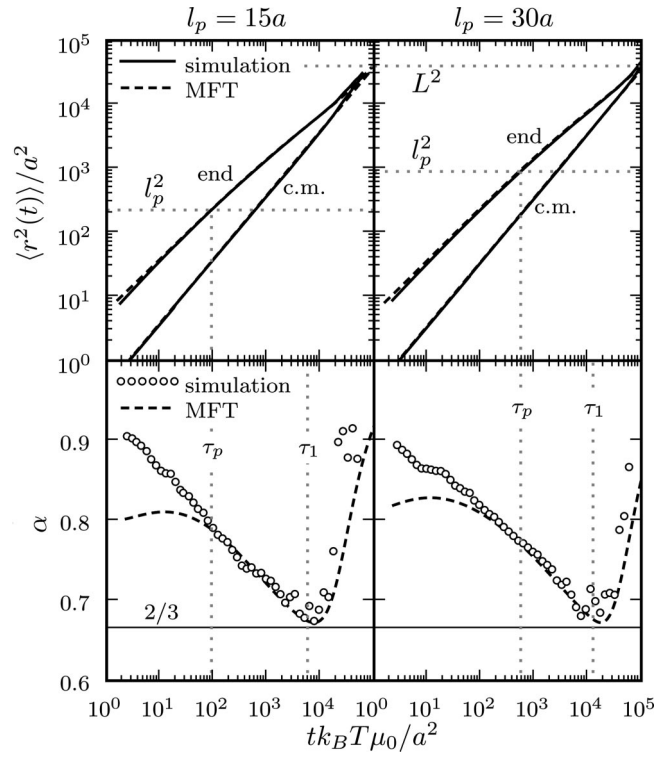

Figure 4. Same as in Figure 3, but for chains of length $L = 200a$ and persistence lengths $l_p = 15a$ and $30a$.

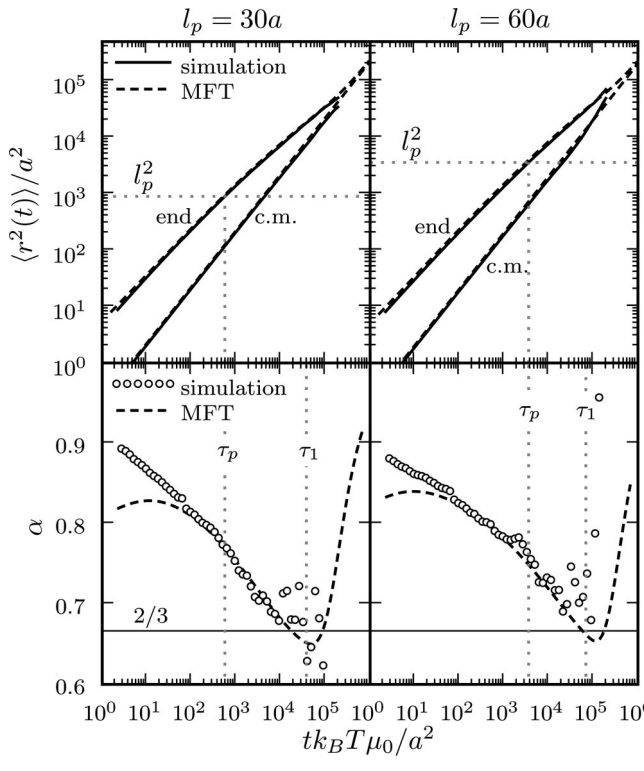

Figure 5. Same as in Figure 3, but for chains of length $L = 400a$ and persistence lengths $l_p = 30a$ and $60a$.

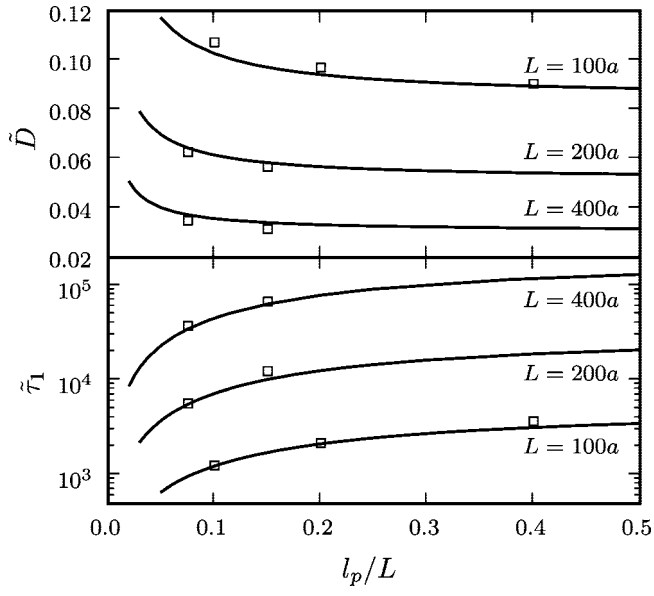

Figure 6. Diffusion constant $\tilde{D} = D/(k_BT\mu_0)$ (top) and longest relaxation time $\tilde{\tau}_1 = \tau_1 k_BT\mu_0/a^2$ (bottom) as a function of l_p/L for three different chain lengths L. The squares are Brownian dynamics simulation results, while the solid curves are calculated from MFT.

shown in Figure 7 for three different chains, with the modified MFT labeled as MFT′. The long-time behavior is unaffected by removing the highest modes, but at short times the MFT′ $\alpha(t)$ curves fit the simulation data much more closely. We rationalize this as being due to an effective cutoff of fluctuations at small wavelengths due to the spring stiffness in the simulation, which is not represented well by the Gaussian MFT elastic energy in eq 17.

In Figure 7 we also show the MSD and $\alpha(t)$ curves calculated using the HWR model. This model follows the same basic

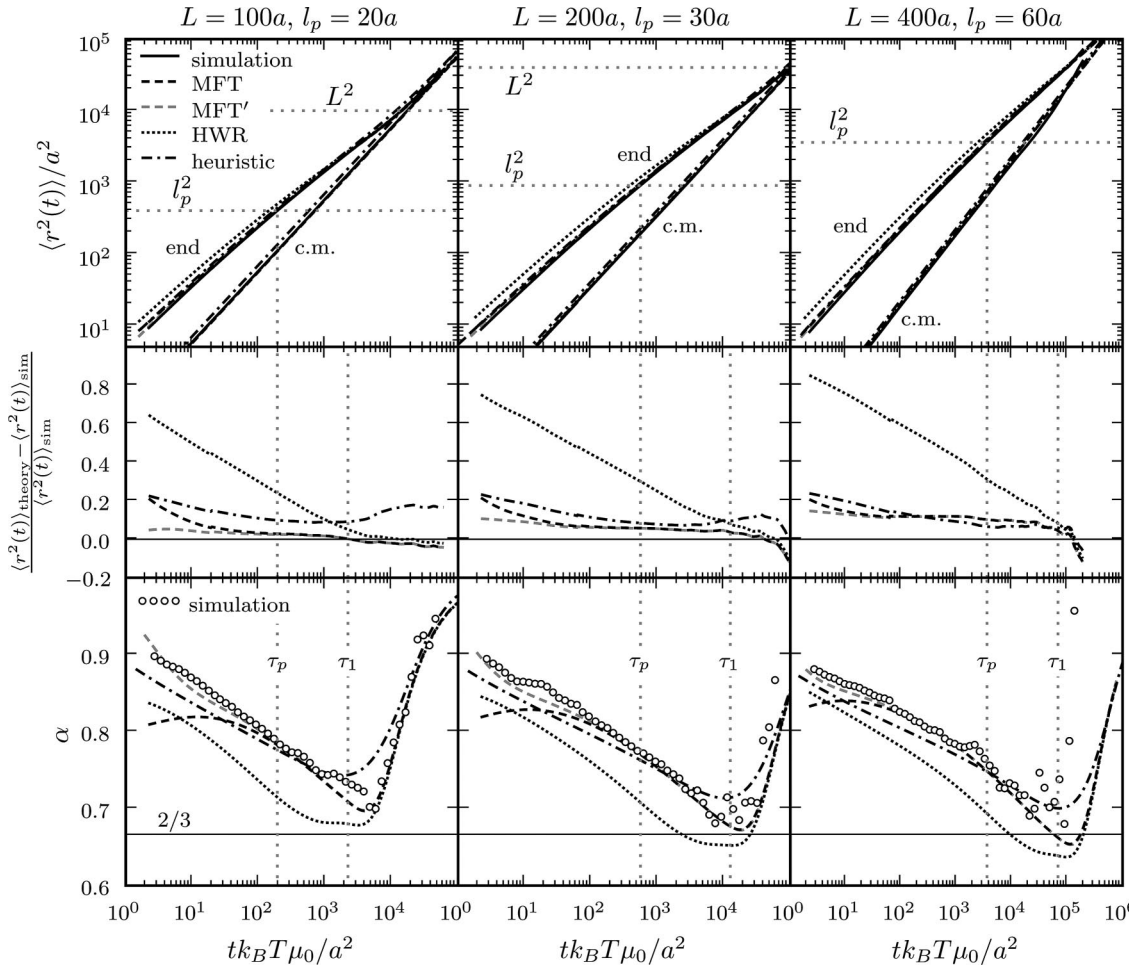

Figure 7. Comparison of the simulation results for three semiflexible chains with several analytical approaches: the heuristic scaling argument described in section 2, the MFT described in section 4, and the MFT′, HWR[9] models described in section 5. The top panels show the end-monomer and center-of-mass MSD $\langle r^2(t)\rangle$; the middle panels show the relative difference between the various theoretical results for the end-monomer MSD and the simulation data; the bottom panels show the local slope $\alpha = \mathrm{d}(\log\langle r^2(t)\rangle)/\mathrm{d}(\log t)$ for the end-monomer MSD. Two times are indicated by dotted vertical lines: τ_p, the time at which the end-monomer $\langle r^2(\tau_p)\rangle = l_p^2$, and τ_1, the longest relaxation time of the polymer. The τ_1 and τ_p values shown are from the numerical simulations.

approach as in section 4, with two additional approximations: (i) only the diagonal elements H_{nn} of eq 34 are used; (ii) for $n > 1$, the H_{nn} are evaluated approximately as[9]

$$H_{nn} \approx 2\sqrt{\frac{6}{\pi}}\frac{\mu_0 a}{L}\int_d^L \mathrm{d}s\,\frac{L-s}{\sqrt{\sigma(s)}}\exp\left(-\frac{3d^2}{2\sigma(s)}\right)\cos\alpha_n s \quad (38)$$

The net effect of these approximations is negligible only for $t \gtrsim \tau_1$, where the HWR and MFT results overlap. For $t < \tau_1$ there are significant differences with respect to the simulations. Here the HWR model overestimates the end-monomer MSD and underestimates $\alpha(t)$. The discrepancy is only slightly reduced by avoiding the approximation of eq 38; the main weakness of the HWR model is that the off-diagonal matrix elements H_{nm} are not included in the calculation. Taking these into account, as the MFT results demonstrate, gives a much more accurate description of the simulation data at short and intermediate times. Despite these differences, the sub-Zimm scaling regime exists in the HWR model, and the deviation below 2/3 is even larger than in the MFT. (The sub-Zimm scaling is also implicitly evident in related quantities calculated from the HWR approach, like the fluorescence correlation function studied in ref 3.)

For comparison, Figure 7 also shows the $\langle r^2(t)\rangle$ and $\alpha(t)$ curves calculated from the heuristic scaling argument of section 2. Despite its simplicity, it is able to capture the trends of the simulation and MFT data quite well, though for shorter chain lengths it gives a shallower dip in α within the intermediate regime.

Given the success of the MFT at reproducing the simulation results, it is interesting to see what the theory predicts for longer chain lengths where Brownian hydrodynamics simulations become impractical. Figure 8a shows $\alpha(t)$ curves for $L = 12000a$, $l_p = 50a-3000a$, with the point $\alpha(\tau_p)$ on each curve marked by a dot. As in the shorter chains, there is a broad dip in $\alpha(t)$ between τ_p and τ_1, but the minimum of $\alpha(t)$ has been shifted to below 2/3. In fact, the dependence of this minimum on L and l_p, illustrated in Figure 8b−d, is qualitatively the same as that derived from the heuristic scaling argument in Figure 1b−d: there is a general trend of $\min_t \alpha$ decreasing with L, and in particular the smallest value possible at a given L, $\min_{l_p} \min_t \alpha$, has a nearly linear dependence on $1/\log(L/a)$ (the heuristic result from Figure 1d is also drawn for reference).

At $l_p = 50a$, corresponding to the persistence length of DNA, $\min_t \alpha$ ranges from 0.698 at $L = 100a$ to 0.617 at $L = 12000a$. (In fact, the minimum saturates at 0.617 in the long chain limit.) Within this range we can make a detailed comparison for three particular chain lengths where experimental MSD data for double-stranded DNA is available from ref 2: $L = 816a$, $2278a$, and $7854a$, or equivalently 2400 bp, 6700 bp, and 23 100 bp (using $a = 1$ nm and a rise per base pair of 0.34 nm). The experimental end-monomer MSD for these three cases is shown in the top panels of Figure 9. The bottom panels show the local

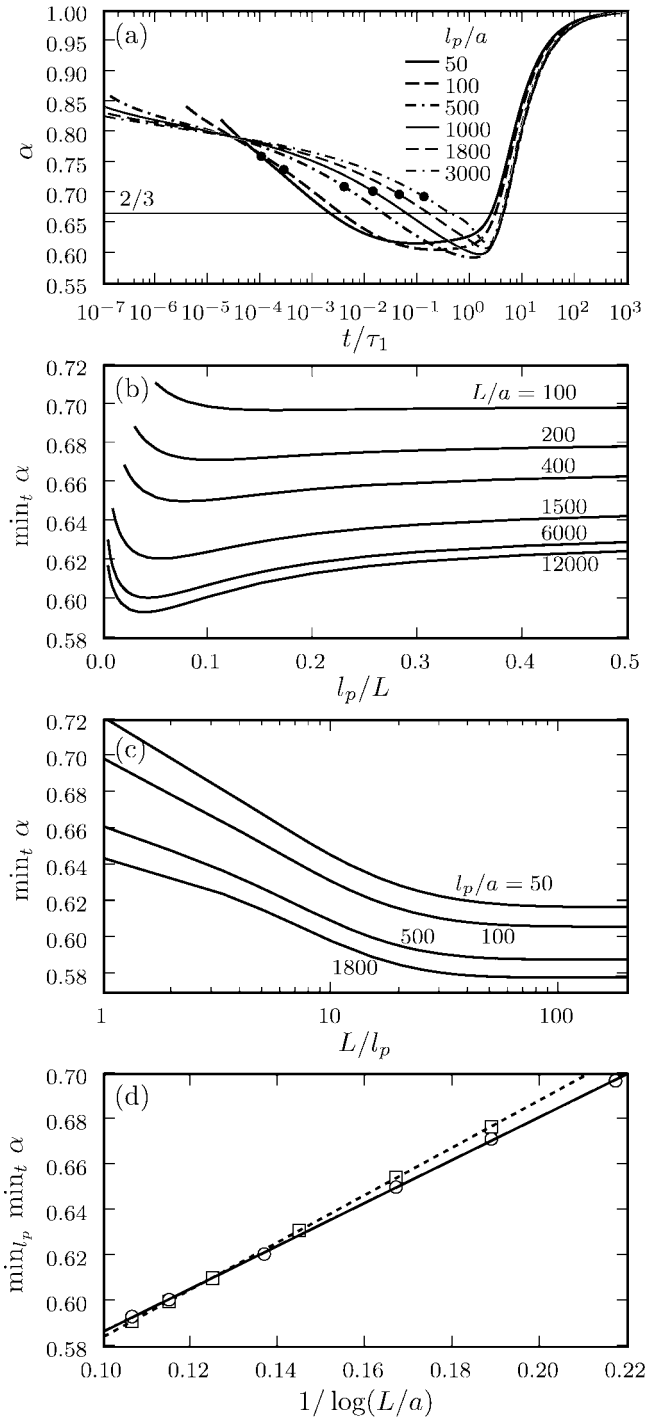

Figure 8. Results of the MFT for various semiflexible chains. (a) The end-monomer MSD effective exponent $\alpha = d(\log\langle r^2(t)\rangle)/d(\log t)$ vs t/τ_1 for polymers of diameter $2a$, contour length $L = 12000a$, and various persistence lengths $l_p = 50a-3000a$. The dot along each $\alpha(t)$ curve marks $\alpha(\tau_p)$. The time τ_p is where $\langle r^2(\tau_p)\rangle = l_p^2$, and τ_1 is the longest relaxation time of the polymer. (b) The minimum value of α over all t vs l_p/L for several chain lengths $L = 100a-12000a$. (c) The minimum value of α over all t vs L/l_p for several $l_p = 50a-1800a$. (d) The circles show the minimum value of α in each of the curves in panel (b), plotted as a function of $1/\log(L/a)$. Superimposed is a straight-line fit to the data points, $0.49 + 0.95/\log(L/a)$. The squares, with the dashed straight-line fit, are the corresponding results of the heuristic scaling argument, taken from Figure 1d.

slope $\alpha(t)$, which can be estimated at each t by fitting straight lines to the log−log plot of MSD data points with times t_i within a small range around t, defined by the condition $|\log t_i/t| < 0.15$. Together with the experimental results for the MSD and $\alpha(t)$ are the curves predicted by the MFT and heuristic scaling argument. Besides the length scale parameters mentioned above, the other dimensional variables in the system are set at the following values (taken from the literature and the experimental conditions): $l_p = 50$ nm, $T = 293$ K, viscosity of water at 293 K = 1 mPa s. At longer times (>10 ms) there is quite good agreement between both theories and experimental data, particularly notable since there is no fitting parameter involved in the MFT. The discrepancies arise in the short and intermediate time regime, where the experimental MSD is consistently higher than the theoretical one, the difference increasing to roughly a factor of 2−3 at the shortest times measured. The discrepancy in the MSD is on the order of 0.001−0.01 μm^2, corresponding to length scales roughly 30−100 nm. Experimental data seem to indicate faster displacement of the end monomer at very short times followed by slower increase of the MSD at intermediate times compared to the theoretical predictions.

The effect of the higher experimental MSD is to push the local slope down relative to the theoretical value. Thus, the intermediate dynamical regime, in the range 0.01−10 ms, is characterized by a broad region with $\alpha(t)$ close to 0.5, in contrast to the MFT results where $\min_t \alpha$ is between 0.633 for $L = 2400$ bp and 0.617 for $L = 23\,100$ bp. Though there are large uncertainties in the experimental data for $t < 0.01$ ms (on average 50% for $L = 2400$ bp, going down to 10% for $L = 23\,100$ bp), the rough trend in the local slope appears to show a rapid increase in $\alpha(t)$ as t is decreased. This rapid crossover again contrasts with the MFT curve, where the increase in the local slope is more gradual. The heuristic scaling results support the MFT: with the crossover exponents and fitting constants set at the values shown below eq 6, the heuristic $\langle r^2(t)\rangle$ almost perfectly overlaps with the MFT curve in all three cases, and the local slopes are consequently also very similar. Independently, we also checked if it was possible to find an alternative set of fitting parameters which would make the heuristic $\langle r^2(t)\rangle$ agree with the experimental data, but we were unable to obtain a reasonable fit.

Although the existence of an intermediate regime with sub-Zimm scaling is found in both experiment and theory, the quantitative discrepancy of the scaling behavior points to a gap between the experimental system and the theoretical approaches. Possibly, a semiflexible polymer model based on a wormlike chain is sufficient only for describing the large-scale motions of the DNA. There may be some missing elements in the theory (for example, an additional degree of freedom present in DNA, like torsional dynamics) that lead to faster motion at shorter scales. On the other hand, there is also the possibility that limitations in the setup and analysis of FCS measurements could contribute to the discrepancy. Deviations from the assumed Gaussian profile of the confocal detection volume and uncertainties in the diffusion coefficient of the rhodamine molecule used to calibrate the shape of this volume have been shown by alternative methods like two-focus FCS to lead to substantial systematic errors in the single-focus setup.[28] The uncertainties in the FCS analysis are highlighted by the differing results produced by independent studies of similar double-stranded DNA systems: one yielding a substantial sub-Zimm regime,[2] with local exponents near the Rouse limit, and others giving a smaller deviation below the Zimm value over shorter time ranges,[3,5] as fitted by the HWR model. Regardless of these issues, there is one aspect in which both the experimental and theoretical approaches agree: an intermediate dynamical regime is present in the end-monomer MSD results, and this regime shows sub-Zimm scaling for long enough chains.

6. Discussion

To understand the intermediate dynamical regime in more detail, and to see where the deviations from the Zimm model

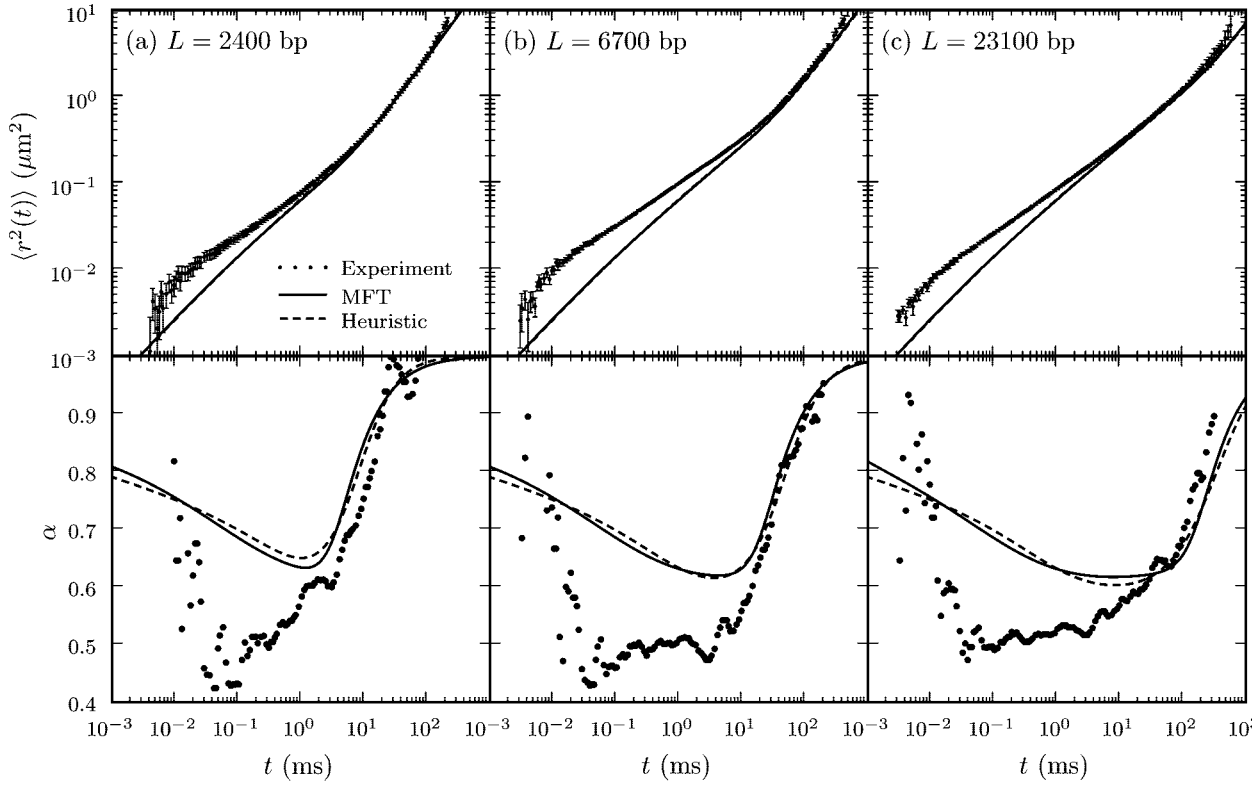

Figure 9. Comparison of the MFT and heuristic scaling results to experimental MSD data taken from ref 2 for three lengths of double-stranded DNA: (a) 2400 bp; (b) 6700 bp; (c) 23 100 bp. The dimensional parameters in the theories are fixed at $a = 1$ nm, rise per bp = 0.34 nm, $l_p = 50$ nm, $T = 293$ K, and viscosity of water at 293 K = 1 mPa s. The top panels show the end-monomer MSD $\langle r^2(t)\rangle$, and the bottom panels show the corresponding effective local exponent $\alpha = \mathrm{d}(\log\langle r^2(t)\rangle)/\mathrm{d}(\log t)$.

arise, let us analyze the behavior of eq 37, whose general form is shared by any theory that expresses the end-monomer MSD in terms of contributions from normal modes. Both τ_n and Δ_n decrease approximately as power laws in n, and we can describe this decrease through effective local exponents γ_n, $\delta_n > 1$:

$$\gamma_n = -\frac{\mathrm{d}\log\tau_n}{\mathrm{d}\log n}, \quad \delta_n = -\frac{\mathrm{d}\log\Delta_n}{\mathrm{d}\log n} \tag{39}$$

Several examples of τ_n and Δ_n are plotted in Figure 10 for $L = 12000a$ and $l_p = 50a-3000a$. The variation of γ_n and δ_n with n is shown in the insets. The behavior of the MSD slope $\alpha(t)$ can be directly related to these local exponents. Let us assume that within some time range $\tau_{n_2} \ll t \ll \tau_{n_1}$, $n_2 \gg n_1$, the associated normal mode exponents are approximately constant: $\gamma_n \approx \gamma$, $\delta_n \approx \delta$ for $n_1 < n < n_2$. Then the dominant contribution to the subdiffusive behavior at times t within this range is given by

$$\begin{aligned}\langle r^2(t)\rangle &\approx \sum_{n=n_1}^{n_2} \Delta_n(1 - \mathrm{e}^{-t/\tau_n}) \\ &\approx \Delta_{n_1} n_1^{\delta} \int_{n_1}^{\infty} \mathrm{d}n\, n^{-\delta}(1 - \exp(-tn^{\gamma}/\tau_{n_1} n_1^{\gamma})) \\ &= \Delta_{n_1} n_1 \left(\frac{1}{\delta - 1} + \frac{1}{\gamma} E_{1+(\delta-1)/\gamma}(t/\tau_{n_1})\right)\end{aligned} \tag{40}$$

In the second line we extended the upper limit of the integration from n_2 to ∞ using the fact that $t \gg \tau_{n_2}$, $n_2 \gg n_1$, and in the third line $E_\nu(x)$ denotes the exponential integral function, $E_\nu(z) \equiv \int_1^\infty \mathrm{d}t \exp(-zt)/t^\nu$. For $t \ll \tau_{n_1}$, eq 40 can be expanded to the leading order as

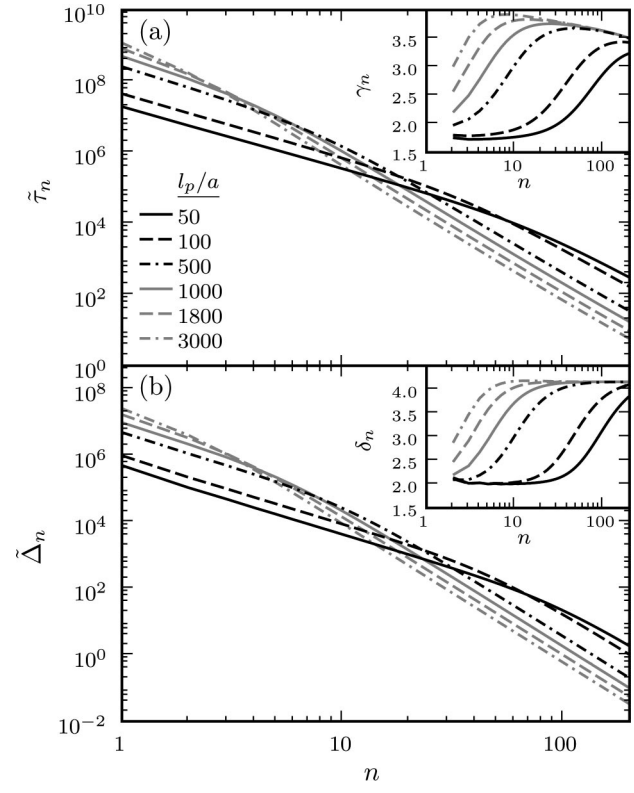

Figure 10. Values of (a) $\tilde{\tau}_n = \tau_n k_B T \mu_0/a^2$, (b) $\tilde{\Delta}_n = \Delta_n/a^2$ as a function of mode number n for a semiflexible polymer of length $L = 12000a$ with various $l_p = 50a-3000a$, calculated using MFT. The parameters Δ_n and relaxation times τ_n determine the subdiffusive behavior of the end-monomer MSD through eq 37. The insets show the effective local exponents describing the scaling of τ_n and Δ_n with n: $\gamma_n = -\mathrm{d}(\log\tau_n)/\mathrm{d}(\log n)$, $\delta_n = -\mathrm{d}(\log\Delta_n)/\mathrm{d}(\log n)$.

$$\langle r^2(t)\rangle \approx \frac{\Delta_{n_1} n_1}{\delta - 1}\Gamma\left(\frac{1-\delta+\gamma}{\gamma}\right)\left(\frac{t}{\tau_{n_1}}\right)^{(\delta-1)/\gamma} \quad (41)$$

This implies that for $\tau_{n_2} \ll t \ll \tau_{n_1}$ the local slope is given by $\alpha(t) \approx (\delta - 1)/\gamma$. As can be seen in the insets of Figure 10, there are two distinct regimes for γ_n and δ_n: one for modes $n \ll L/l_p$, corresponding to length scales greater than l_p, and another for modes $n \gg L/l_p$, corresponding to length scales smaller than l_p. A continuous crossover occurs from one regime to the other for $n \sim O(L/l_p)$. These two regimes in turn lead to differing behaviors for $\alpha(t)$. We will consider each regime separately, focusing on earlier predictions for each case and how they compare to the present results.

Modes with $n \ll L/l_p$ correspond to internal polymer dynamics on length scales between l_p and L, and this is precisely the intermediate dynamical regime that we have mentioned earlier. In the simplest analysis, ignoring hydrodynamical effects, these modes should be described by the Rouse model, particularly in the flexible limit of small n where the length scales are much greater than l_p. The Rouse theory yields the following expressions for τ_n and Δ_n[7]

$$\tau_n^{\text{Rouse}} = \frac{L^2 b^2}{12\pi^2 k_B T \mu_0 a^2} n^{-2}, \quad \Delta_n^{\text{Rouse}} = \frac{2Lb^2}{a\pi^2} n^{-2} \quad (42)$$

where b is the Kuhn length, $b = r_{ee}^2(L)/L$. The local exponents in the Rouse model are constants: $\delta_n = 2$ and $\gamma_n = 2$. Using eq 41, we find the following asymptotic behavior for the end-monomer MSD:

$$\langle r^2(t)\rangle \approx \Delta_1^{\text{Rouse}}\Gamma(1/2)(t/\tau_1^{\text{Rouse}})^{1/2} = \left(\frac{48 b^2 k_B T \mu_0}{\pi}\right)^{1/2} t^{1/2} \quad (43)$$

This is the origin of the Rouse scaling result $\alpha(t) = 1/2$. In the presence of hydrodynamic interactions, the Zimm model is expected to hold, with eq 42 modified as[7]

$$\tau_n^{\text{Zimm}} = \frac{b^3 (L/\pi a)^{3/2}}{12\sqrt{6} k_B T \mu_0 a} n^{-3/2}, \quad \Delta_n^{\text{Zimm}} = \Delta_n^{\text{Rouse}} \quad (44)$$

Here the local exponent γ_n is 3/2, and thus the asymptotic behavior of the MSD becomes

$$\langle r^2(t)\rangle \approx \frac{12\Gamma(1/3)(2ak_B T\mu_0)^{2/3}}{\pi} t^{2/3} \quad (45)$$

leading to the Zimm scaling $\alpha(t) = 2/3$.

The MFT calculations, however, give a different picture, deviating from the Zimm result. Consider the chain in Figure 10 closest to the flexible limit: $L = 12000a$, $l_p = 50a$. The exponents γ_n and δ_n are approximately constant for $n \lesssim 10$ but are shifted from the Zimm values: $\gamma \approx 1.74$, $\delta \approx 2.04$ averaged over $n = 1-10$, giving $\alpha = (\delta - 1)/\gamma \approx 0.60$. Indeed, in the corresponding local slope curve plotted in Figure 8a the $\alpha(t)$ value is nearly constant over the time scales associated with these modes ($t/\tau_1 \approx 0.018-1$), reaching a minimum of 0.617. It is these shifts in γ_n and δ_n from the Zimm theory predictions that lead to an intermediate dynamical regime for longer chains where $\alpha(t) < 2/3$.

To get an analytical estimate for these shifts within the framework of the MFT theory, one can approximately evaluate the integrals for the interaction matrix elements H_{nm} in eq 34 and account for the effects of the off-diagonal elements using perturbation theory. The details of the approximation can be found in Appendix B. For $n \ll L/l_p$ the results are

$$\gamma_n \approx \frac{3p_1(n) + 5.07p_2(n)\sqrt{\frac{nl_p}{L}}K\left(\frac{6a^2}{l_p^2}\right)}{2p_3(n) + 2.89p_4(n)\sqrt{\frac{nl_p}{L}}K\left(\frac{6a^2}{l_p^2}\right)}$$

$$\delta_n \approx \frac{2p_5(n) + 0.0393p_6(n)\sqrt{\frac{l_p}{nL}}K\left(\frac{6a^2}{l_p^2}\right)}{p_7(n) + 0.0157p_8(n)\sqrt{\frac{l_p}{nL}}K\left(\frac{6a^2}{l_p^2}\right)} \quad (46)$$

where $K(x) \equiv (6/\pi)^{1/2}(E_1(x) - E_1(3/2)) - 4(3/\pi)^{1/2} + 2$, and $p_1(n),\ldots, p_8(n)$ are polynomials in n of the form $p_i(n) = 1 + a_i/n + b_i/n^2 + \ldots$, with coefficients a_i and b_i given in Table 1. For $L \gg a$ and l_p approaching the flexible limit, $l_p \to 2a$, the first terms in the numerators and denominators of the γ_n and δ_n expressions dominate, and thus there is a range of modes $1 \ll n \ll L/l_p$ where $\gamma_n \approx 3/2$ and $\delta_n \approx 2$, in agreement with the expected Zimm scaling for a flexible chain. However, for a semiflexible chain where $l_p \gg a$, corrections to the Zimm values become more important. Using the fact that $E_1(z) \approx -\log z$ as $z \to 0$, the $K(6a^2/l_p^2)$ terms in the γ_n expression lead to a positive shift of order $(nl_p/L)^{1/2}\log(l_p/a)$. For δ_n the shift upward is smaller, of order $(l_p/nL)^{1/2}\log(l_p/a)$. These corrections due to semiflexibility are evident in the exact numerical results for chains of length $L = 12000a$ shown in the insets of Figure 10, particularly for $l_p = 50a$ and $100a$ where a $n \ll L/l_p$ regime is identifiable. As expected from the analytical approximation, the deviation in γ_n from the Zimm value is more significant than that of δ_n. In fact, the averages of γ_n and δ_n for $n = 1-10$ from the approximate expressions in eq 46 are 1.68 and 2.06, respectively, comparable to the numerical results 1.74 and 2.04 quoted above.

In the other regime, for modes with $n \gg L/l_p$, the oscillations are at length scales smaller than l_p, where the rigidity of the chain is the dominating factor. For this case it is easiest to consider first the MFT in the absence of hydrodynamic interactions and then see how the final results are modified when the interactions are included. In the free-draining limit, the interaction matrix $H_{nm} = 2a\mu_0\delta_{nm}$, and for large n the constants α_n in eqs 31 and 32 are approximately $\alpha_n \approx n\pi/L$.[9] With these simplifications we find

$$\tau_n \approx \frac{L^4}{3a\mu_0 l_p k_B T \pi^4} n^{-4}, \quad \Delta_n \approx \frac{16L^3}{l_p \pi^4} n^{-4} \quad (47)$$

for $n \gg L/l_p$. Thus $\delta_n = \gamma_n = 4$. Plugging these results into eq 41 gives

$$\langle r^2(t)\rangle \approx \frac{16\Gamma(1/4)}{\pi}\frac{(a\mu_0 k_B T)^{3/4}}{(3l_p)^{1/4}} t^{3/4} \quad (48)$$

Table 1. Coefficients a_i and b_i of Polynomials $p_i(n) = 1 + a_i/n + b_i/n^2 + \cdots$

i	1	2	3	4	5	6	7	8
a_i	−0.176	−0.0919	−0.297	−0.148	0.282	0.608	0.188	0.435
b_i	−0.00186	−0.00504	0.0179	−0.00196	0.0440	0.185	0.0220	0.103

for the end-monomer MSD. The scaling $\langle r^2(t)\rangle \sim t^{3/4}$ is a well-known property of monomer motion in the stiff-rod limit, as seen in theory[9−14,29] simulations,[15,30,31] and experiments.[4,32−36] Though hydrodynamic effects are typically expected to induce only weak logarithmic corrections in this limit, we find that including these effects in the MFT does have an observable consequence. In the insets of Figure 10 all the γ_n and δ_n curves appear to overlap for $n \gg L/l_p$, but their values are shifted away from 4: γ_n gradually decreases with n, varying between 3.9 and 3.5 in the range shown, and $\delta_n \approx 4.15-4.2$. The behavior of γ_n and δ_n leads to $\alpha(t) > 3/4$ in this regime, as is seen most clearly in the large l_p results in Figure 8a, which exhibit a broad region where the $\alpha(t)$ curves converge over the range 0.8−0.85 for $t \ll \tau_p$.

The MFT analytical estimate for the $n \gg L/l_p$ case, using the approximation detailed in Appendix B, gives

$$\gamma_n \approx 4 + \frac{12}{A - 12\log\left(\frac{L}{an\pi}\right)}$$

$$\delta_n \approx 4 + \frac{24}{\left(3 + A - 12\log\left(\frac{L}{an\pi}\right)\right)\left(5 + A - 12\log\left(\frac{L}{an\pi}\right)\right)} \tag{49}$$

where the constant $A = 18\gamma - 2(6\pi)^{1/2} + 6E_1(3/2) + 6\log(6) \approx 13.06$ and $\gamma \approx 0.5772$ is Euler's constant. The functional forms for γ_n and δ_n in eq 49, independent of l_p, describe the curves toward which all the γ_n and δ_n results in the insets of Figure 10 converge for sufficiently large n, with γ_n shifted below 4 and δ_n shifted above 4. The gradual decrease in γ_n with n is similar to an earlier theoretical approach where hydrodynamics was explicitly considered: in ref 11 the relaxation times for a stiff-rod were found to scale like $\tau_n \propto n^{-4}/\log(L/an\pi)$, corresponding to $\gamma_n = 4 - 1/\log(L/an\pi)$.

In a more intuitive fashion, the heuristic scaling developed in section 2 allows to trace back the deviations from the traditional Zimm and wormlike chain scaling results in eqs 45 and 48 to the slow crossovers in the diffusion and spatial size of subchain segments.

7. Conclusion

Between the flexible and stiff-rod limits hydrodynamic interactions modify the scaling of the end-monomer MSD in ways that are not accounted for in the Zimm model or in earlier semiflexible polymer theories. In particular, there exists an intermediate dynamical regime for sufficiently long polymers with local exponent $\alpha(t)$ between 2/3 and 1/2, the Zimm and Rouse predictions. We have investigated this regime through a wormlike chain model, in conjunction with a variety of theoretical techniques: Brownian hydrodynamics simulations for shorter chain lengths, supplemented by mean-field theory with hydrodynamic preaveraging for longer chains where the simulations are not practical. In the cases where both MFT and numerical results are available, there is very good quantitative agreement between them. The two approaches are further supported by a heuristic scaling argument that can accurately capture the trends in $\langle r^2(t)\rangle$ and $\alpha(t)$ and that allows us to connect the observed sub-Zimm scaling regime to previous scaling approaches developed for the stiff-rod and the flexible-chain limits. Note that previous less accurate mean-field approaches that were used to analyze the FCS data of ref 5 give a sub-Zimm scaling range even more pronounced than found by us.

Though the MFT and heuristics show a noticeable dip below the Zimm exponent of 2/3 at intermediate times, they do not reach the Rouse-like value of 1/2 seen in the experimental double-stranded DNA results of ref 2. Comparison between the experimental data and the theory raises a important issue: while the long-time data, corresponding to the large-scale dynamics of the DNA, is described surprisingly well by the MFT, serious discrepancies arise at shorter times. The small-scale motions revealed by experiment are significantly faster than predicted, indicating either a deficiency in the simple wormlike chain description or in the analysis of the FCS measurements. Further work is thus necessary in order to gain a complete understanding of the monomer dynamics of DNA in solution.

Acknowledgment. This research was supported by the Deutscher Akademischer Austausch Dienst (DAAD) program "Research Stays for University Academics and Scientists" and by the Scientific and Technical Research Council of Turkey (TÜBITAK). M.H. thanks Pamir Talazan of the Feza Gürsey Research Institute for assistance with the Gilgamesh computing cluster, on which the numerical simulations were carried out. M.R. acknowledges financial support of the National Science Foundation under Grants CHE-0616925 and CBET-0609087 and the National Institutes of Health under Grant 1-R01-HL0775486A. O.K. acknowledges support by Israel Science Foundation Grant 663/04. M.R., R.N., and O.K. thank the Kavli Institute for Theoretical Physics for initiating the collaboration.

Appendix A. Mean-Field Theory of an Extensible Wormlike Chain

As an alternative to the mean-field theory of section 4, which begins with the inextensible Kratky−Porod chain of eq 12, we can derive a mean-field model based on the extensible wormlike chain Hamiltonian used in the Brownian dynamics simulations, eqs 10 and 11, thus making explicit the relationship between the simulation and analytical results. Ignoring the Lennard-Jones term, the simulation Hamiltonian has the form

$$U = \frac{\gamma}{4a}\sum_{i=1}^{M-1}(r_{i+1,i} - 2a)^2 + \frac{\epsilon}{2a}\sum_{i=2}^{M-1}(1 - \cos\theta_i)$$

$$= \frac{\Gamma}{2d}\sum_{i=1}^{M-1}(u_i - 1)^2 + \frac{\epsilon}{d}\sum_{i=2}^{M-1}\left(1 - \frac{\mathbf{u}_i\cdot\mathbf{u}_{i-1}}{u_i u_{i-1}}\right) \tag{50}$$

where $d = 2a$, $\Gamma = \gamma d^2$, and $\mathbf{u}_i = (\mathbf{r}_{i+1} - \mathbf{r}_i)/d$. For large Γ (the case in the simulations), the values of $u_i = |\mathbf{u}_i| \approx 1$, and we can expand $(u_i - 1)^2 = ([1 + (u_i^2 - 1)]^{1/2} - 1)^2 \approx (u_i^2 - 1)^2/4 + O((u_i^2 - 1)^3)$. Keeping the leading term, we rewrite eq 50 as

$$U \approx \frac{\Gamma}{8d}\sum_{i=1}^{M-1}(u_i^2 - 1)^2 - \frac{\epsilon}{d}\sum_{i=2}^{M-1}\mathbf{u}_i\cdot\mathbf{u}_{i-1} + \frac{\epsilon}{d}(M - 2) \tag{51}$$

Neglecting the last term of eq 51, since it is a constant, the chain partition function Z is given by

$$Z = \int\prod_{i=1}^{M-1}\mathrm{d}\mathbf{u}_i\, \mathrm{e}^{-\beta U}$$

$$= \int\prod_{i=1}^{M-1}\mathrm{d}\mathbf{u}_i \exp\left(-\frac{\beta\Gamma}{8d}\sum_{i=1}^{M-1}(u_i^2-1)^2 + \frac{\beta\epsilon}{d}\sum_{i=2}^{M-1}\mathbf{u}_i\cdot\mathbf{u}_{i-1}\right) \tag{52}$$

We can rewrite the integrand of Z using the relations

$$\mathrm{e}^{-\frac{\beta\Gamma}{8d}(u_i^2-1)^2} \propto \int_{-i\infty}^{i\infty}\mathrm{d}\lambda_i\, \mathrm{e}^{-\beta\lambda_i d(u_i^2-1)+\frac{2\beta d^3}{\Gamma}\lambda_i^2} \tag{53}$$

and $\mathbf{u}_i\cdot\mathbf{u}_{i-1} = {}^1\!/_2(u_i^2 + u_{i-1}^2 - (\mathbf{u}_i - \mathbf{u}_{i-1})^2)$, where we have introduced an auxiliary variable λ_i for each i. The result, up to a constant prefactor, is

$$Z = \int_{-i\infty}^{i\infty} \prod_{i=1}^{M-1} \mathrm{d}\lambda_i \, \mathrm{e}^{-\beta F(\{\lambda_i\})} \tag{54}$$

with

$$F(\{\lambda_i\}) = -\beta^{-1} \log \int \prod_{i=1}^{M-1} \mathrm{d}\mathbf{u}_i \, \mathrm{e}^{-\beta U(\{\lambda_i\})} \tag{55}$$

and

$$U(\{\lambda_i\}) = d\sum_{i=2}^{M-2}\left(\lambda_i - \frac{\epsilon}{d^2}\right)u_i^2 + \frac{\epsilon}{2d}\sum_{i=2}^{M-1}(\mathbf{u}_i - \mathbf{u}_{i-1})^2 + d\left(\lambda_1 - \frac{\epsilon}{2d^2}\right)u_i^2 + d\left(\lambda_{M-1} - \frac{\epsilon}{2d^2}\right)u_{M-1}^2 - d\sum_{i=1}^{M-1}\lambda_i - \frac{2d^3}{\Gamma}\sum_{i=1}^{M-1}\lambda_i^2 \tag{56}$$

To derive a mean-field model, we can now apply a stationary phase approximation analogous to the one used in section 4:[23,24]

$$Z = \int_{-i\infty}^{i\infty} \prod_{i=1}^{M-1} \mathrm{d}\lambda_i \mathrm{e}^{-\beta F(\{\lambda_i\})} \approx \mathrm{e}^{-\beta F(\{\lambda_i^{\mathrm{cl}}\})} \tag{57}$$

where $\{\lambda_i^{\mathrm{cl}}\}$ satisfy

$$\left.\frac{\partial F}{\partial \lambda_i}\right|_{\{\lambda_i=\lambda_i^{\mathrm{cl}}\}} = 0, \quad i = 1, ..., M-1 \tag{58}$$

From symmetry, we know λ_i^{cl} must have the property $\lambda_i^{\mathrm{cl}} = \lambda_{M-i}^{\mathrm{cl}}$ for all i, and thus we can write the solution to eq 58 in the form

$$\lambda_i^{\mathrm{cl}} = \nu_i + \frac{\epsilon}{d^2}, \quad i = 2, ..., M-2$$
$$\lambda_1^{\mathrm{cl}} = \lambda_{M-1}^{\mathrm{cl}} = \frac{\nu_0}{d} + \frac{\epsilon}{2d^2} \tag{59}$$

for some set of values $\{\nu_i\}$ and ν_0, where $\nu_i = \nu_{M-i}$. This yields a mean-field free energy

$$F_{\mathrm{MF}} \equiv F(\{\lambda_i^{\mathrm{cl}}\}) = -\beta^{-1} \log \int \prod_{i=1}^{M-1} \mathrm{d}\mathbf{u}_i \, \mathrm{e}^{-\beta U_{\mathrm{MF}}} \tag{60}$$

with

$$U_{\mathrm{MF}} = d\sum_{i=2}^{M-2}\nu_i u_i^2 + \frac{\epsilon}{2d}\sum_{i=2}^{M-1}(\mathbf{u}_i - \mathbf{u}_{i-1})^2 + \nu_0(u_1^2 + u_{M-1}^2) - d\sum_{i=2}^{M-2}\nu_i - 2\nu_0 - \frac{2d^3}{\Gamma}\sum_{i=2}^{M-2}\left(\nu_i + \frac{\epsilon}{d^2}\right)^2 - \frac{4d^3}{\Gamma}\left(\frac{\nu_0}{d} + \frac{\epsilon}{2d^2}\right)^2 \tag{61}$$

In the continuum limit $d \to 0$, $M \to \infty$, $Md \to L$ and we replace $\mathbf{u}_i$, ν_i by continuous functions $\mathbf{u}(s)$, $\nu(s)$ of the contour variable s. Assuming the Hamiltonian parameters ϵ and Γ remain fixed in this limit, we have

$$F_{\mathrm{MF}} = -\beta^{-1} \log \int \mathscr{D}u \, \mathrm{e}^{-\beta U_{\mathrm{MF}}}$$
$$U_{\mathrm{MF}} = \int_{-L/2}^{L/2} ds \, \nu(s)\mathbf{u}^2(s) + \frac{\epsilon}{2}\int_{-L/2}^{L/2} \mathrm{d}s\left(\frac{\partial \mathbf{u}(s)}{\partial s}\right)^2 + \nu_0(\mathbf{u}^2(L/2) + \mathbf{u}^2(-L/2)) - \int_{-L/2}^{L/2} \mathrm{d}s \, \nu(s) - 2\nu_0 - \frac{4\epsilon}{\Gamma}\int_{-L/2}^{L/2} \mathrm{d}s \, \nu(s) - \frac{4\nu_0\epsilon}{\Gamma} - C \tag{62}$$

where $C = \lim_{d\to 0}(2L\epsilon^2/\Gamma d^2 + \epsilon^2/\Gamma d)$ is an infinite constant independent of $\nu(s)$ and ν_0. The stationary point condition eq 58 becomes

$$\frac{\delta F_{\mathrm{MF}}}{\delta \nu(s)} = 0, \quad \frac{\partial F_{\mathrm{MF}}}{\partial \nu_0} = 0 \tag{63}$$

Physically, eq 63 implies the following constraints:

$$\langle \mathbf{u}^2(s)\rangle = 1 + \frac{4\epsilon}{\Gamma}, \qquad -L/2 < s < L/2$$
$$\langle \mathbf{u}^2(-L/2)\rangle = \langle \mathbf{u}^2(L/2)\rangle = 1 + \frac{2\epsilon}{\Gamma} \tag{64}$$

where $\langle ... \rangle$ denotes the thermal average with respect to the Hamiltonian U_{MF}. As expected, the magnitude of the tangent vector fluctuations become smaller as the extensibility parameter Γ increases, going to the limit $\langle \mathbf{u}^2(s)\rangle = 1$ for all s when $\Gamma \to \infty$. As will be seen below, in this limit the present theory reproduces the results of section 4.

Unfortunately, eq 63 is not analytically tractable because the F_{MF} given by eq 62 cannot be evaluated in closed form for an arbitrary function $\nu(s)$. On the other hand, the stationary point condition in the discrete system, eq 58 for F in eq 55, can be solved numerically for small M, and a representative set of ν_i are shown in Figure 11 (for $M = 20$, $\epsilon = 10k_{\mathrm{B}}Td$, $\Gamma = 400k_{\mathrm{B}}Td$). For large $\Gamma \gg \epsilon$, the ν_i are nearly constant for $2 \le i \le M-2$, and we can use this fact to make the following approximation in the continuum limit: replace $\nu(s)$ by a constant ν in the Hamiltonian U_{MF} of eq 62. Thus, the first part of eq 63 becomes $\partial F_{\mathrm{MF}}/\partial \nu = 0$, implying a global constraint

$$\int_{-L/2}^{L/2} \mathrm{d}s \, \langle \mathbf{u}^2(s)\rangle = \left(1 + \frac{4\epsilon}{\Gamma}\right)L \tag{65}$$

instead of the local constraint $\langle \mathbf{u}^2(s)\rangle = 1 + 4\epsilon/\Gamma$ in eq 64.

This approximation, which becomes exact when $\Gamma \to \infty$, allows us to find a closed form expression for F_{MF}. Using a mapping of the first two terms of U_{MF} to the quantum mechanical harmonic oscillator (with mass $m = \epsilon$ and frequency $\omega = (2\nu/\epsilon)^{1/2}$),[23] the path integral for F_{MF} can be evaluated, giving the free energy

$$F_{\mathrm{MF}} = -L\nu - 2\nu_0 - \frac{4L\nu\epsilon}{\Gamma} - \frac{4\nu_0\epsilon}{\Gamma} - \frac{3}{2\beta}\left(\log\left[\beta\sqrt{\nu\epsilon}\,\mathrm{csch}\left(L\sqrt{\frac{2\nu}{\epsilon}}\right)\right] - \log\left[\frac{\beta^2(2\nu_0{}^2 + \nu\epsilon)}{2} + \beta^2\nu_0\sqrt{2\nu\epsilon}\coth\left(L\sqrt{\frac{2\nu}{\epsilon}}\right)\right]\right) \tag{66}$$

up to an additive constant. Using eq 66, the stationary point condition $\partial F_{\mathrm{MF}}/\partial \nu = \partial F_{\mathrm{MF}}/\partial \nu_0 = 0$ can be solved numerically

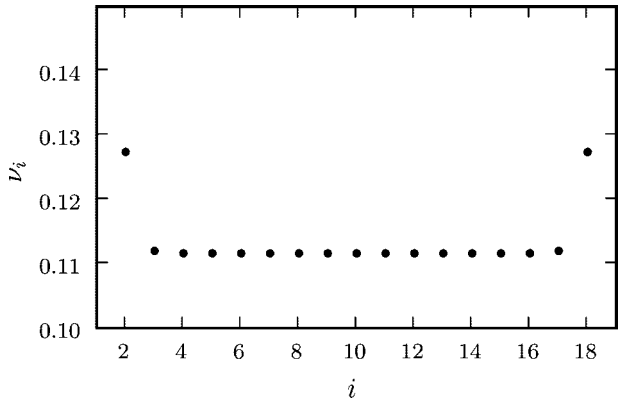

Figure 11. Numerical solution to the stationary point condition eq 58 for a system with $M = 20$, $\epsilon = 10k_BTd$, and $\Gamma = 400k_BTd$. The solution is expressed in terms of $\nu_i = \lambda_i^{cl} - \epsilon/d^2$ for $i = 2,..., M-2$, in units of k_BT/d. The value of $\nu_0/d = \lambda_1^{cl} - \epsilon/2d^2 = \lambda_{M-1}^{cl} - \epsilon/2d^2$ is $0.7831k_BT/d$.

for ν and ν_0 given L, ϵ, and Γ. For $L \gg \epsilon$, the condition takes the simple limiting form

$$\sqrt{\frac{\nu\epsilon}{2}} = \frac{3}{4}k_BT\frac{\Gamma}{\Gamma + 4\epsilon}$$
$$\nu_0 = \frac{3}{4}k_BT\frac{\Gamma(\Gamma + 6\epsilon)}{(\Gamma + 2\epsilon)(\Gamma + 4\epsilon)} \tag{67}$$

When $\Gamma \to \infty$, eq 67 reduces to eq 18 in section 4, and this is generally true of the stationary point condition for any L.

The equilibrium properties of the chain described by the Hamiltonian U_{MF} can be calculated with a similar approach to the one used in ref 27, where distribution functions were derived for the $\Gamma = \infty$ mean-field model. The main result is $G(s, s'; \mathbf{x}; \mathbf{u}, \mathbf{u}')$, the probability density for finding two points on the chain at s and s' with $s' > s$, having spatial separation $\mathbf{r}(s') - \mathbf{r}(s) = \mathbf{x}$, and tangent vectors $\mathbf{u}(s) = \mathbf{u}$, $\mathbf{u}(s') = \mathbf{u}'$. The full expression for this probability is

$$G(s, s'; \mathbf{x}; \mathbf{u}, \mathbf{u}') = \left(\frac{A(s, s')}{4\pi^3 B_4(s' - s)}\right)^{3/2} \exp[-B_1(s' - s) \times$$
$$(\mathbf{u}^2 + \mathbf{u}'^2) + B_2(s' - s)\mathbf{u}\cdot\mathbf{u}' - \frac{(\mathbf{x} - B_3(s' - s)(\mathbf{u} + \mathbf{u}'))^2}{B_4(s' - s)} -$$
$$C(s + L/2)\mathbf{u}^2 - C(L/2 - s')\mathbf{u}'^2] \tag{68}$$

where the functions $A(s)$, $B_i(s)$, $i = 1,..., 4$, and $C(s)$ are given by

$$A(s, s') = 4(B_1(s' - s) + C(s + L/2))(B_1(s' - s) +$$
$$C(L/2 - s')) - B_2^2(s' - s)$$
$$B_1(s) = \frac{\beta\epsilon\omega}{2}\coth(s\omega)$$
$$B_2(s) = \beta\epsilon\omega\,\mathrm{csch}(s\omega)$$
$$B_3(s) = \frac{\epsilon\omega}{2\nu}\tanh\left(\frac{s\omega}{2}\right) \tag{69}$$
$$B_4(s) = \frac{s}{\beta\nu} - \frac{\epsilon\omega}{\beta\nu^2}\tanh\left(\frac{s\omega}{2}\right)$$
$$C(s) = \frac{\beta\epsilon\omega(\epsilon\omega + 2\nu_0\coth(s\omega))}{4\nu_0 + 2\varepsilon\omega\coth(s\omega)}$$

with $\omega = (2\nu/\epsilon)^{1/2}$.

From $G(s, s'; \mathbf{x}; \mathbf{u}, \mathbf{u}')$ we can calculate other properties of the chain, for example, the tangent vector correlation function $\langle \mathbf{u}(s)\cdot\mathbf{u}(s')\rangle$ for $s' > s$

$$\langle \mathbf{u}(s)\cdot\mathbf{u}(s')\rangle = \int d^3\mathbf{x}\mathbf{u}(s)\cdot\mathbf{u}(s')G(s, s'; \mathbf{x}; \mathbf{u}(s), \mathbf{u}(s'))$$
$$= \frac{B_2(s' - s)}{A(s', s)} \tag{70}$$

For $L \gg \epsilon$, $-L/2 \ll s, s' \ll L/2$, eq 70 can be simplified using eq 67 for ν and ν_0, giving

$$\langle \mathbf{u}(s)\cdot\mathbf{u}(s')\rangle = \left(1 + \frac{4\epsilon}{\Gamma}\right)\exp\left(-\frac{3(s' - s)\Gamma k_BT}{2\epsilon(\Gamma + 4\epsilon)}\right) \tag{71}$$

When $\Gamma \to \infty$, the tangent correlation function reduces to the Kratky−Porod form of eq 19, $\langle \mathbf{u}(s)\cdot\mathbf{u}(s')\rangle = \exp(-3(s' - s)k_BT/2\epsilon) = \exp(-(s' - s)/l_p)$.

Thus, we have shown that a mean-field theory based on the extensible wormlike chain Hamiltonian used in the simulations gives results very similar to the MFT described in section 4, with the finite extensibility leading to small corrections to the parameters of U_{MF} on the order of ϵ/Γ.

Appendix B. Analytical Approximation for γ_n and δ_n

In order to derive analytical expressions for the exponents γ_n and δ_n from the MFT theory, we make several approximations in the derivation described in section 44. Since the off-diagonal elements of the interaction matrix H_{nm} defined by eq 34 are smaller than the diagonal ones, we will treat them as a perturbation. To first order in the perturbation expansion, we can write the following expressions for τ_n, Θ_n, and $\Psi_n(L/2)$ when $n > 0$:

$$\tau_n = \Lambda_n^{-1}$$
$$\approx \lambda_n^{-1}H_{nn}^{-1} - H_{nn}^{-2}\lambda_n^{-1}\sum_{m\neq n}\frac{H_{nm}^2\lambda_m}{H_{nn}\lambda_n - H_{mm}\lambda_m}$$
$$\Theta_n \approx H_{nn} + 2\sum_{m\neq n}\frac{H_{nm}^2\lambda_m}{H_{nn}\lambda_n - H_{mm}\lambda_m}$$
$$\Psi_n(L/2) = \sum_m \psi_m(L/2)(C^{-1})_{mn} \approx \psi_n(L/2) + \sqrt{\frac{1}{L}}\frac{H_{0n}}{H_{nn}} +$$
$$\sum_{m\neq n}\psi_m(L/2)\frac{H_{nm}\lambda_n}{H_{nn}\lambda_n - H_{mm}\lambda_m} \tag{72}$$

From these expressions one can also calculate $\Delta_n = 6k_BT\tau_n\Theta_n\Psi_n^2(L/2)$. The double integral for H_{nm} in eq 34 can be rewritten in terms of new variables $h = s - s'$ and $w = s + s'$ as follows:

$$H_{nm} = 2a\mu_0\delta_{nm} + \sqrt{\frac{6}{\pi}}a\mu_0\int_{-L/2}^{L/2}ds\int_{-L/2}^{L/2}ds'\,\psi_n(s) \times$$
$$\frac{\Theta(|s - s'| - 2a)}{\sqrt{\sigma(|s - s'|)}}\exp\left(-\frac{6a^2}{\sigma(|s - s'|)}\right)\psi_m(s')$$
$$= 2a\mu_0\delta_{nm} + \sqrt{\frac{6}{\pi}}a\mu_0\int_{2a}^{L}dh\int_{-L+h}^{L-h}dw$$
$$\psi_n\left(\frac{h + w}{2}\right)\frac{1}{\sqrt{\sigma(h)}}\exp\left(-\frac{6a^2}{\sigma(h)}\right)\psi_m\left(\frac{w - h}{2}\right) \tag{73}$$

Since $\sigma(h) = 2l_ph - 2l_p^2(1 - e^{-h/l_p})$ can be approximated as $\sigma(h) \approx h^2$ for $h \ll l_p$ and $\sigma(h) \approx 2l_ph$ for $h \gg l_p$, we can split up the h integral above into two pieces:

$$H_{nm} \approx 2a\mu_0\delta_{nm} + a\mu_0(I^{(1)}_{nm} + I^{(2)}_{nm}) \tag{74}$$

where

$$I^{(1)}_{nm} = \sqrt{\frac{6}{\pi}}\int_{2a}^{l_p} \mathrm{d}h \frac{1}{h}\exp\left(-\frac{6a^2}{h^2}\right)\times \int_{-L+h}^{L-h} \mathrm{d}w\, \psi_n\left(\frac{h+w}{2}\right)\psi_m\left(\frac{w-h}{2}\right)$$
$$I^{(2)}_{nm} = \sqrt{\frac{6}{\pi}}\int_{l_p}^{L} \mathrm{d}h \frac{1}{\sqrt{2l_p h}}\exp\left(-\frac{3a^2}{l_p h}\right)\times \int_{-L+h}^{L-h} \mathrm{d}w\, \psi_n\left(\frac{h+w}{2}\right)\psi_m\left(\frac{w-h}{2}\right) \tag{75}$$

To complete the approximation, we will estimate these integrals in the two mode regimes discussed in section 6, one for the case $n \ll L/l_p$ and the other for $n \gg L/l_p$. Since the biggest perturbation contributions in eq 72 for τ_n, Θ_n, and $\Psi_n(L/2)$ come from states with m in the vicinity of n, it is sufficient to consider matrix elements H_{mn} for m in the same mode regime as n.

B.1. $n, m \ll L/l_p$ Regime. In the limit of long chain lengths, where $L \gg l_p, a$, the functions $\psi_n(s)$ and constants α_n, λ_n for $0 < n \ll L/l_p$ in eqs 31 and 32 simplify to

$$\psi_n(s) \approx \begin{cases} (-1)^{(n-1)/2}\sqrt{\frac{2}{L}}\sin\left(\frac{\pi n s}{L}\right) & n \text{ odd} \\ (-1)^{n/2}\sqrt{\frac{2}{L}}\cos\left(\frac{\pi n s}{L}\right) & n \text{ even} \end{cases}$$
$$\alpha_n \approx \frac{\pi n}{L}$$
$$\lambda_n \approx \frac{3k_B T\pi^2 n^2}{2l_p L^2} \tag{76}$$

Because of the symmetry of the $\psi_n(s)$ functions, the matrix elements H_{nm} are nonzero only when n and m are both odd or both even, so the perturbation expansions in eq 72 can be done independently for even and odd states. For simplicity, we will assume n and m are odd for the rest of the derivation. Carrying out the analogous approximation for even n, m, will lead to qualitatively similar final expressions for δ_n and γ_n, with slight shifts in the numerical coefficients.

Plugging eq 76 into eq 75, we can approximately evaluate the integrals in the large L limit:

$$I^{(1)}_{nm} \approx \begin{cases} \frac{4\sqrt{6}}{L\sqrt{\pi}}[2a\mathrm{e}^{-3/2} - l_p\mathrm{e}^{-6a^2/l_p^2} + a\sqrt{6\pi}\,\mathrm{erf}(\sqrt{3/2}) - a\sqrt{6\pi}\,\mathrm{erf}(\sqrt{6}a/l_p)] & n \neq m \\ \sqrt{\frac{6}{\pi}}[E_1(6a^2/l_p^2) - E_1(3/2)] & n = m \end{cases}$$
$$I^{(2)}_{nm} \approx \begin{cases} -\sqrt{\frac{L}{l_p}}\frac{2\sqrt{6}}{(n+m)(\sqrt{n}+\sqrt{m})\pi^{3/2}} & n \neq m \\ \sqrt{\frac{6L}{\pi l_p}}\left(\frac{1}{n^{1/2}} - \frac{1}{2\pi n^{3/2}}\right) - 2\sqrt{\frac{12}{\pi}} & n = m \end{cases} \tag{77}$$

Plugging these results into eq 74 for H_{nm}, we can also estimate the sums involved in the perturbation expansion of eq 72:

$$\sum_{m\neq n}\frac{H^2_{nm}\lambda_m}{H_{nn}\lambda_n - H_{mm}\lambda_m} \approx \sqrt{\frac{L}{l_p}}\left(\frac{-108\pi + 27\pi^2}{18\sqrt{6}\pi^{7/2}n^{3/2}} + \frac{-126 + 72\pi - 16\sqrt{3}\pi}{18\sqrt{6}\pi^{7/2}n^{5/2}}\right)$$
$$\sum_{m\neq n}\psi_m(L/2)\frac{H_{nm}\lambda_n}{H_{nn}\lambda_n - H_{mm}\lambda_m} \approx \sqrt{\frac{2}{L}}\left[\frac{1}{18}(-9 + 4\sqrt{3}) + \frac{-9 + (9+\sqrt{3})\pi}{27\pi^2 n} - \frac{72 - 45\pi + 4\sqrt{3}\pi}{216\pi^3 n^2}\right] \tag{78}$$

Combining the results of eqs 72, 74, and 76−78, we can derive the following expressions for γ_n and δ_n:

$$\gamma_n = -\frac{\mathrm{d}\log\tau_n}{\mathrm{d}\log n} = -\frac{n}{\tau_n}\frac{\mathrm{d}\tau_n}{\mathrm{d}n} \approx \frac{3p_1(n) + 5.07p_2(n)\sqrt{\frac{nl_p}{L}}K\left(\frac{6a^2}{l_p^2}\right)}{2p_3(n) + 2.89p_4(n)\sqrt{\frac{nl_p}{L}}K\left(\frac{6a^2}{l_p^2}\right)}$$
$$\delta_n = -\frac{\mathrm{d}\log\Delta_n}{\mathrm{d}\log n} = -\frac{n}{\Delta_n}\frac{\mathrm{d}\Delta_n}{\mathrm{d}n} \approx \frac{2p_5(n) + 0.0393p_6(n)\sqrt{\frac{l_p}{nL}}K\left(\frac{6a^2}{l_p^2}\right)}{p_7(n) + 0.0157p_8(n)\sqrt{\frac{l_p}{nL}}K\left(\frac{6a^2}{l_p^2}\right)} \tag{79}$$

where

$$K(x) \equiv \sqrt{\frac{6}{\pi}}(E_1(x) - E_1(3/2)) - 4\sqrt{\frac{3}{\pi}} + 2 \tag{80}$$

and $p_1(n)$, ..., $p_8(n)$ are polynomials in n of the form $p_i(n) = 1 + a_i/n + b_i/n^2 + \ldots$. The first two coefficients a_i and b_i are given in Table 1.

B.2. $n, m \gg L/l_p$ Regime. With the assumptions that $L \gg l_p$ and $l_p \gg a$, the functions $\psi_n(s)$ and constants α_n, λ_n for $n \gg L/l_p$ in eqs 31 and 32 become

$$\psi_n(s) \approx \begin{cases} (-1)^{(n-1)/2}\sqrt{\frac{2}{L}}\sin\left(\frac{\pi(2n-1)s}{2L}\right) + \sqrt{\frac{1}{L}}\frac{\sinh(\pi(2n-1)s/2L)}{\cosh(\pi(2n-1)/4)} & n \text{ odd} \\ (-1)^{n/2}\sqrt{\frac{2}{L}}\cos\left(\frac{\pi(2n-1)s}{2L}\right) + \sqrt{\frac{1}{L}}\frac{\cosh(\pi(2n-1)s/2L)}{\sinh(\pi(2n-1)/4)} & n \text{ even} \end{cases}$$
$$\alpha_n \approx \frac{\pi(2n-1)}{2L}$$
$$\lambda_n \approx \frac{3k_B T l_p \pi^4 (2n-1)^4}{32L^4} \tag{81}$$

Again we will focus for simplicity on the case of odd n and m. For $n, m \gg L/l_p$, the first integral in eq 75 dominates, $I^{(1)}_{nm} \gg I^{(2)}_{nm}$, so we can write $H_{nm} \approx 2a\mu_0\delta_{nm} + a\mu_0 I^{(1)}_{nm}$. The integral $I^{(1)}_{nm}$ can be approximated as

$$I^{(1)}_{nm} \approx \begin{cases} (m^2+n^2)\left(\log\left(\frac{16a^2mn\pi^2}{L^2}\right)+2\gamma\right) - \\ \frac{2\sqrt{6}}{\pi^{3/2}}\frac{(m+n-1)(m+n)^2\pi}{(m+n-1)(m+n)(m^2+n^2)} & n \neq m \\ -\frac{\sqrt{6}}{n\pi^{3/2}}\left[3+n\pi\left\{3\gamma+E_1\left(\frac{3}{2}\right)+2\log\left(\frac{\sqrt{6}a\pi n}{L}\right)\right\}\right] & n = m \end{cases} \tag{82}$$

where $\gamma \approx 0.5772$ is Euler's constant. The resulting sums in the perturbation expansion of eq 72 are

$$\sum_{m\neq n}\frac{H^2_{nm}\lambda_m}{H_{nn}\lambda_n - H_{mm}\lambda_m} \approx \frac{12\sqrt{6}}{n\sqrt{\pi}\left(3+A-12\log\left(\frac{L}{an\pi}\right)\right)}$$

$$\sum_{m\neq n}\psi_m(L/2)\frac{H_{nm}\lambda_n}{H_{nn}\lambda_n - H_{mm}\lambda_m} \approx \frac{2}{\sqrt{L}}\left(\frac{1}{3+A-12\log\left(\frac{L}{an\pi}\right)}\right) \tag{83}$$

where the constant $A = 18\gamma - 2(6\pi)^{1/2} + 6E_1(3/2) + 6\log(6) \approx 13.06$. This yields the following expressions for γ_n and δ_n:

$$\gamma_n \approx 4 + \frac{12}{A-12\log\left(\frac{L}{an\pi}\right)}$$

$$\delta_n \approx 4 + \frac{24}{\left(3+A-12\log\left(\frac{L}{an\pi}\right)\right)\left(5+A-12\log\left(\frac{L}{an\pi}\right)\right)} \tag{84}$$

References and Notes

(1) Lumma, D.; Keller, S.; Vilgis, T.; Rädler, J. O. *Phys. Rev. Lett.* **2003**, *90*, 218301.
(2) Shusterman, R.; Alon, S.; Gavrinyov, T.; Krichevsky, O. *Phys. Rev. Lett.* **2004**, *92*, 048303.
(3) Winkler, R. G.; Keller, S.; Rädler, J. O. *Phys. Rev. E* **2006**, *73*, 041919.
(4) Bernheim-Groswasser, A.; Shusterman, R.; Krichevsky, O. *J. Chem. Phys.* **2006**, *125*, 084903.
(5) Petrov, E. P.; Ohrt, T.; Winkler, R. G.; Schwille, P. *Phys. Rev. Lett.* **2006**, *97*, 258101.
(6) Zimm, B. H. *J. Chem. Phys.* **1956**, *24*, 269.
(7) Doi, M.; Edwards, S. F. *The Theory of Polymer Dynamics*; Clarendon Press: Oxford, 1986.
(8) Lisy, V.; Tothova, J.; Zatovsky, A. *Condens. Matter Phys.* **2006**, *9*, 95.
(9) Harnau, L.; Winkler, R. G.; Reineker, P. *J. Chem. Phys.* **1996**, *104*, 6355.
(10) Kroy, K.; Frey, E. *Phys. Rev. E* **1997**, *55*, 3092.
(11) Granek, R. *J. Phys. II* **1997**, *7*, 1761.
(12) Rubinstein, M.; Colby, R. H. *Polymer Physics*; Oxford University Press: Oxford, 2003; pp 322−334.
(13) Morse, D. C. *Phys. Rev. E* **1998**, *58*, R1237.
(14) Gittes, F.; MacKintosh, F. C. *Phys. Rev. E* **1998**, *58*, R1241.
(15) Everaers, R.; Jülicher, F.; Ajdari, A.; Maggs, A. C. *Phys. Rev. Lett.* **1999**, *82*, 3717.
(16) Schlagberger, X.; Bayer, J.; Rädler, J. O.; Netz, R. R. *Europhys. Lett.* **2006**, *76*, 346.
(17) Tirado, M. M.; Martinez, C.; Garcia, J. *J. Chem. Phys.* **1984**, *81*, 2047.
(18) Netz, R. R.; Andelman, D. *Phys. Rep.* **2003**, *380*, 1.
(19) Ermak, D. L. *Rapp. Act. Sci. CECAM* **1976**, 66–81.
(20) Ermak, D. L.; McCammon, J. A. *J. Chem. Phys.* **1978**, *69*, 1352.
(21) Rotne, J.; Prager, S. *J. Chem. Phys.* **1969**, *50*, 4831.
(22) Kratky, O.; Porod, G. *Recl. Trav. Chim. Pays-Bas* **1949**, *68*, 1106.
(23) Ha, B.-Y.; Thirumalai, D. *J. Chem. Phys.* **1995**, *103*, 9408.
(24) Ha, B.-Y.; Thirumalai, D. *J. Chem. Phys.* **1997**, *106*, 4243.
(25) Lagowski, J. B.; Noolandi, J.; Nickel, B. *J. Chem. Phys.* **1991**, *95*, 1266.
(26) Harris, R. A.; Hearst, J. E. *J. Chem. Phys.* **1966**, *44*, 2595.
(27) Winkler, R. G.; Reineker, P.; Harnau, L. *J. Chem. Phys.* **1994**, *101*, 8119.
(28) Dertinger, T.; Pacheco, V.; von der Hocht, I.; Hartmann, R.; Gregor, I.; Enderlein, J. *ChemPhysChem* **2007**, *8*, 433.
(29) Farge, E.; Maggs, A. C. *Macromolecules* **1993**, *26*, 5041.
(30) Dimitrakopoulos, P. *J. Chem. Phys.* **2003**, *119*, 8189.
(31) Dimitrakopoulos, P. *Phys. Rev. Lett.* **2004**, *93*, 217801.
(32) Piekenbrock, T.; Sackmann, E. *Biopolymers* **1992**, *32*, 1471.
(33) Gisler, T.; Weitz, D. A. *Phys. Rev. Lett.* **1999**, *82*, 1606.
(34) Wong, I. Y.; Gardel, M. L.; Reichman, D. R.; Weeks, E. R.; Valentine, M. T.; Bausch, A. R.; Weitz, D. A. *Phys. Rev. Lett.* **2004**, *92*, 178101.
(35) Xu, J. Y.; Palmer, A.; Wirtz, D. *Macromolecules* **1998**, *31*, 6486.
(36) Caspi, A.; Elbaum, M.; Granek, R.; Lachish, A.; Zbaida, D. *Phys. Rev. Lett.* **1998**, *80*, 1106.

MA802017G